

**Electronic supporting information**

**Binding of anionic Pt(II) complexes in a dedicated organic matrix: towards new binary crystalline composites**

Emilia Kuzniak-Glanowska, Dorota Glosz, Grzegorz Niedzielski, Jędrzej Kobylarczyk, Monika Srebro-Hooper, James G. M. Hooper and Robert Podgajny\*

Table of content

<b>Structural descriptions.....</b>	2
Single crystal X-ray diffraction (SC XRD) measurements .....	2
Powder X-ray diffraction (PXRD) measurements .....	6
<b>Spectroscopic characterization.....</b>	10
Electronic absorption spectroscopy .....	10
Nuclear Magnetic Resonance $^{13}\text{C}$ experiments .....	11
<b>Quantum-chemical calculations .....</b>	12
Computational details .....	12
Additional calculated results .....	13
<b>Crystalline composites characterization.....</b>	23
X-ray diffraction experiments, scanning electron microscopy (SEM) /energy dispersive X-ray spectroscopy (EDS).....	23
FT IR characterization.....	27
Mixed 1-Cl/1-CN <sup>-</sup> crystals – DFT predictions .....	28
<b>References .....</b>	29

## Structural descriptions

### Single crystal X-ray diffraction (SC XRD) measurements

All data for **1-CN<sup>-</sup>** system are taken from Ref. S1 unless stated otherwise.

Table S1. Crystal data and structure refinement for  $(\text{PPh}_4)_2\{\text{[PtCl}_4\text{][HAT(CN)}_6\}\cdot 3\text{MeCN}$  (**1-Cl<sup>-</sup>**),  $(\text{PPh}_4)_2\{\text{[PtBr}_4\text{][HAT(CN)}_6\}\cdot 3\text{MeCN}$  (**1-Br<sup>-</sup>**) and  $(\text{PPh}_4)_2\{\text{[Pt(CN)}_4\text{][HAT(CN)}_6\}\cdot 3\text{MeCN}$  (**1-CN<sup>-</sup>**).

Identification code	<b>1-Cl<sup>-</sup></b>	<b>1-Br<sup>-</sup></b>	<b>1-CN<sup>-</sup></b>
Empirical formula	$\text{C}_{72}\text{H}_{49}\text{Cl}_4\text{N}_{15}\text{P}_2\text{Pt}$	$\text{C}_{72}\text{H}_{49}\text{Br}_4\text{N}_{15}\text{P}_2\text{Pt}$	$\text{C}_{76}\text{H}_{49}\text{N}_{19}\text{P}_2\text{Pt}$
Formula weight	1523.09	1700.93	1485.37
Temperature /K	120	100.0	120
Crystal system	orthorhombic	orthorhombic	orthorhombic
Space group	Pnma	Pnma	Pnma
a /Å	12.7351(4)	12.8291(6)	12.7314
b /Å	29.6484(10)	30.0209(15)	30.6723
c /Å	17.6754(5)	17.6145(9)	17.5126
$\alpha$ /°	90	90	90
$\beta$ /°	90	90	90
$\gamma$ /°	90	90	90
Volume /Å <sup>3</sup>	6673.8(4)	6784.1(6)	6838.7
Z	4	4	4
$\rho_{\text{calc}}$ /g/cm <sup>3</sup>	1.516	1.665	1.443
$\mu$ /mm <sup>-1</sup>	2.367	4.527	-
F(000)	3048	3336	-
Crystal size /mm <sup>3</sup>	$0.25 \times 0.19 \times 0.09$	$0.38 \times 0.09 \times 0.04$	-
Radiation /Å	MoK $\alpha$ ( $\lambda = 0.71073$ )	MoK $\alpha$ ( $\lambda = 0.71073$ )	-
2 $\Theta$ range for data collection /°	4.608 to 50.05	4.624 to 50.052	-
	$-15 \leq h \leq 15$	$-15 \leq h \leq 13$	
Index ranges	$-35 \leq k \leq 26$	$-35 \leq k \leq 34$	-
	$-20 \leq l \leq 20$	$-20 \leq l \leq 20$	
Reflections collected	25256 5994	30430 6098	-
Independent reflections	[ $R_{\text{int}} = 0.0348$ , $R_{\text{sigma}} = 0.0274$ ]	[ $R_{\text{int}} = 0.0521$ , $R_{\text{sigma}} = 0.0350$ ]	-
Data/restraints/parameters	5994/0/436	6098/12/436	-
Goodness-of-fit on $F^2$	1.031	1.057	-
Final R indexes [ $I \geq 2\sigma(I)$ ]	$R_1 = 0.0240$ , $wR_2 = 0.0470$	$R_1 = 0.0462$ , $wR_2 = 0.1093$	-
Final R indexes [all data]	$R_1 = 0.0341$ , $wR_2 = 0.0502$	$R_1 = 0.0701$ , $wR_2 = 0.12065$	-
Largest diff. peak/hole /e Å <sup>-3</sup>	0.57/-0.37	1.79/-2.70	-

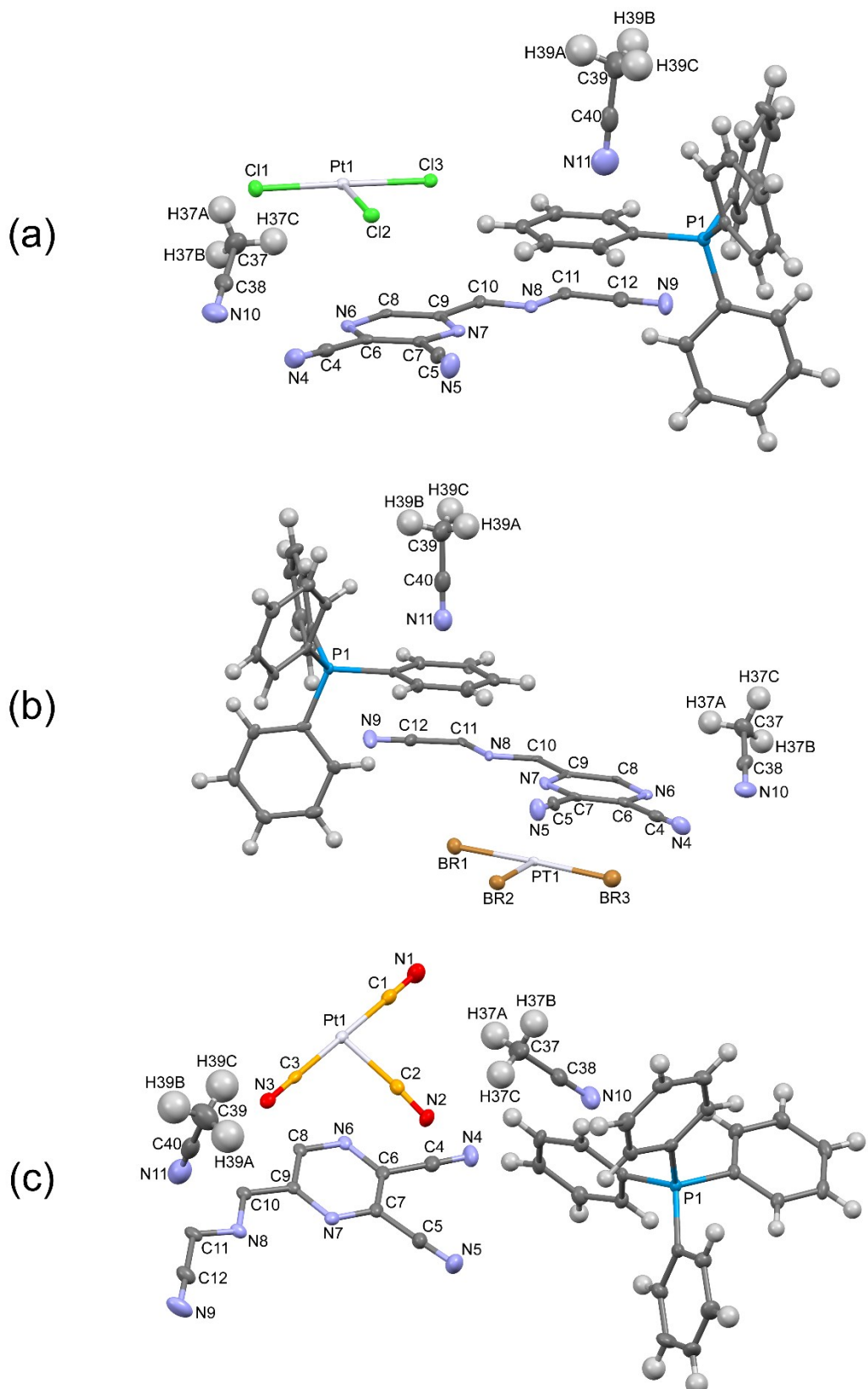


Figure S1. The asymmetric units of **1-Cl<sup>-</sup>** (a), **1-Br<sup>-</sup>** (b) and **1-CN<sup>-</sup>** (c). Colors: Pt – pale grey, P – blue, Cl – green, Br – brown, N – violet, C – dark grey, H – grey, nitrile group: C – orange, N – red. Thermal ellipsoids are drawn at the 50% probability level.

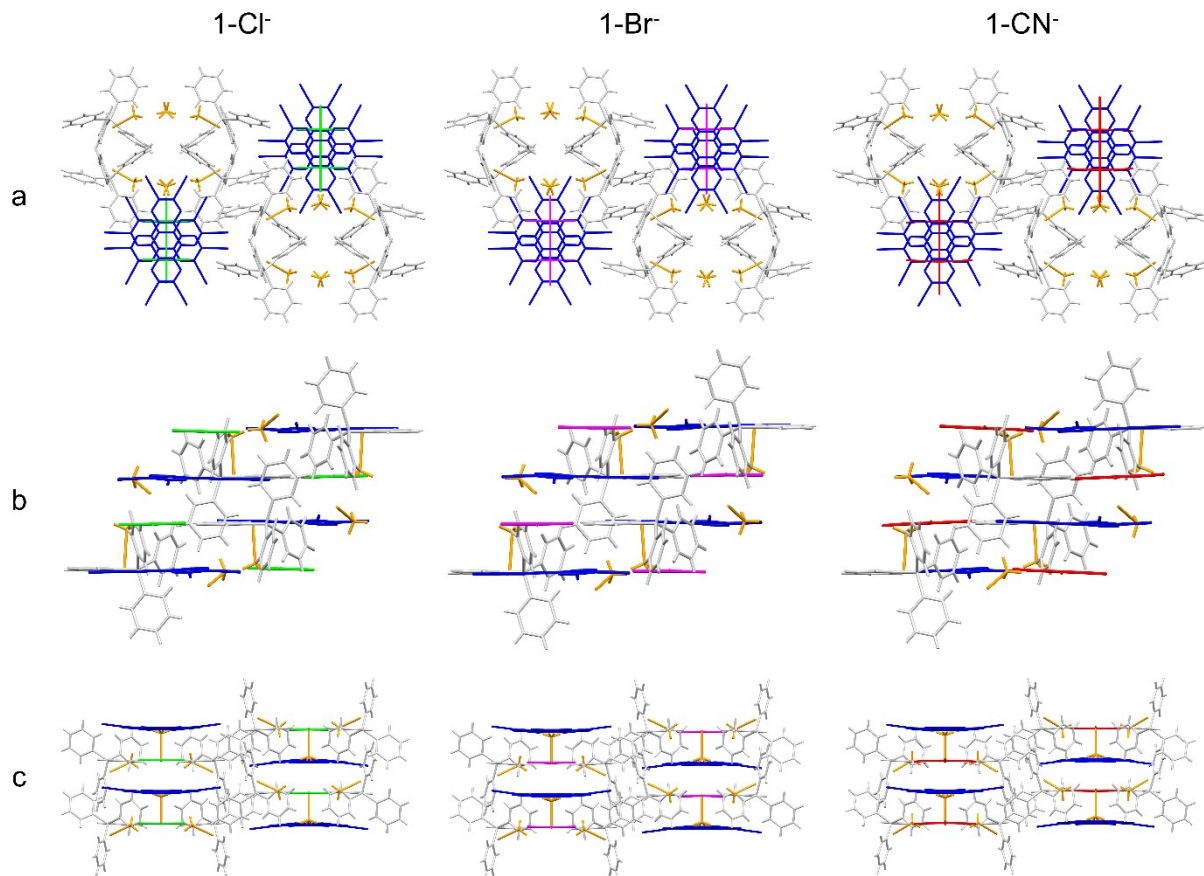


Figure S2. Crystal packing of **1-Cl<sup>-</sup>**, **1-Br<sup>-</sup>** and **1-CN<sup>-</sup>** (columns) along the crystallographic axes *a*, *b* and *c* (rows). Colors: light grey –  $[\text{PPh}_4]^+$ , blue – HAT(CN)<sub>6</sub>, orange – MeCN, red –  $[\text{Pt}(\text{CN})_4]^{2-}$ , pink –  $[\text{PtBr}_4]^{2-}$ , green –  $[\text{PtCl}_4]^{2-}$ .

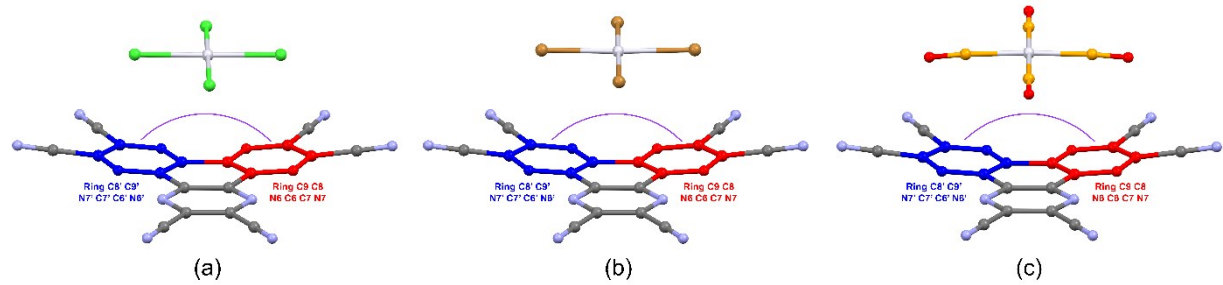


Figure S3. Dihedral angles describing deformation of HAT(CN)<sub>6</sub> molecules in  $(\text{PPh}_4)_2\{[\text{PtCl}_4]\text{HAT}(\text{CN})_6\}\cdot 3\text{MeCN}$  (**1-Cl<sup>-</sup>**) (a),  $(\text{PPh}_4)_2\{[\text{PtBr}_4]\text{HAT}(\text{CN})_6\}\cdot 3\text{MeCN}$  (**1-Br<sup>-</sup>**) (b) and  $(\text{PPh}_4)_2\{[\text{Pt}(\text{CN})_4]\text{HAT}(\text{CN})_6\}\cdot 3\text{MeCN}$  (**1-CN<sup>-</sup>**) (c).

Table S2. Comparison of the selected analogous angles and distances in structures **1-Cl<sup>-</sup>**, **1-Br<sup>-</sup>** and **1-CN<sup>-</sup>**.

No.	<b>1-Cl<sup>-</sup></b>		<b>1-Br<sup>-</sup></b>		<b>1-CN<sup>-</sup></b>	
	Name	Angle/°	Name	Angle/°	Name	Angle/°
<b>1</b>	Cl1 / Pt / Cl3	178.99(3)	Br1 / Pt / Br3	178.42(4)	centr. C1 N1 / Pt / centr. C3 N3	179.96
<b>2</b>	Cl2 / Pt / Cl2'	178.76(3)	Br2 / Pt / Br2'	177.48(4)	centr. C2 N2 / Pt / centr. C2' N2'	175.16
<b>3</b>	planeRing C8' C9' N7' C7' C6' N6'/ planeRing C9 C8 N6 C6 C7 N7	10.22	planeRing C8' C9' N7' C7' C6' N6'/ planeRing C9 C8 N6 C6 C7 N7	9.05	planeRing C8' C9' N7' C7' C6' N6'/ /planeRing C9 C8 N6 C6 C7 N7	9.73
No.	<b>1-Cl<sup>-</sup></b>		<b>1-Br<sup>-</sup></b>		<b>1-CN<sup>-</sup></b>	
	Name	Length/Å	Name	Length/Å	Name	Length/Å
<b>1</b>	Pt --- Cl1	2.3109(9)	Pt --- Br1	2.4268(11)	Pt --- centr. C1 N1 (Pt --- N1)	2.578 (3.152)
<b>2</b>	Pt --- Cl2	2.3166(6)	Pt --- Br2	2.4275(7)	Pt --- centr. C2 N2 (Pt --- N2)	2.572 (3.145)
<b>3</b>	Pt --- Cl3	2.3175(9)	Pt --- Br3	2.4003(13)	Pt --- centr. C3 N3 (Pt --- N3)	2.571 (3.149)
<b>4</b>	Cl1---Pt---Cl3	4.628	Br1---Pt---Br3	4.827	centr. C1 N1---Pt ---centr. C3 N3 (N1---Pt---N3)	5.148 (6.301)
<b>5</b>	Cl2---Pt---Cl2'	4.633	Br2---Pt---Br2'	4.854	centr. C2 N2---Pt ---centr. C2' N2' (N2---Pt---N2')	5.140 (6.282)

## Powder X-ray diffraction (PXRD) measurements

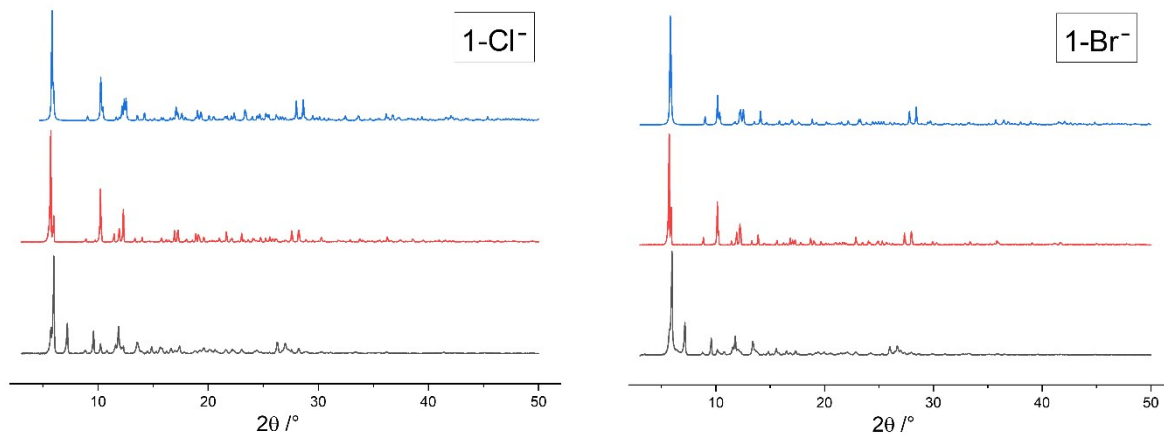


Figure S4. PXRD patterns for **1-Cl<sup>-</sup>** and **1-Br<sup>-</sup>** in 3-50° range of 2 $\Theta$  angle; experimental, sample immersed in mother solution (red lines) and dried samples (black lines), RT; calculated from single crystal X-ray model, 120 K (blue lines).

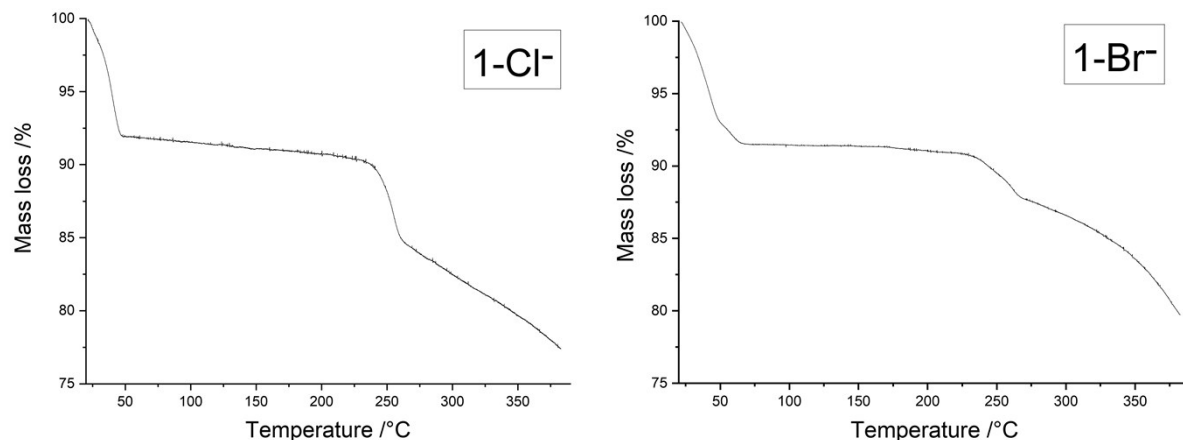


Figure S5. Thermogravimetric analysis for **1-Cl<sup>-</sup>** and **1-Br<sup>-</sup>**. The exact quantitative analysis of TGA curves is hampered due to the observed removal of the crystallization solvent molecules at RT in the ambient conditions.

## Structural description of $(\text{PPh}_4)_2[\text{PtBr}_4]$ salt

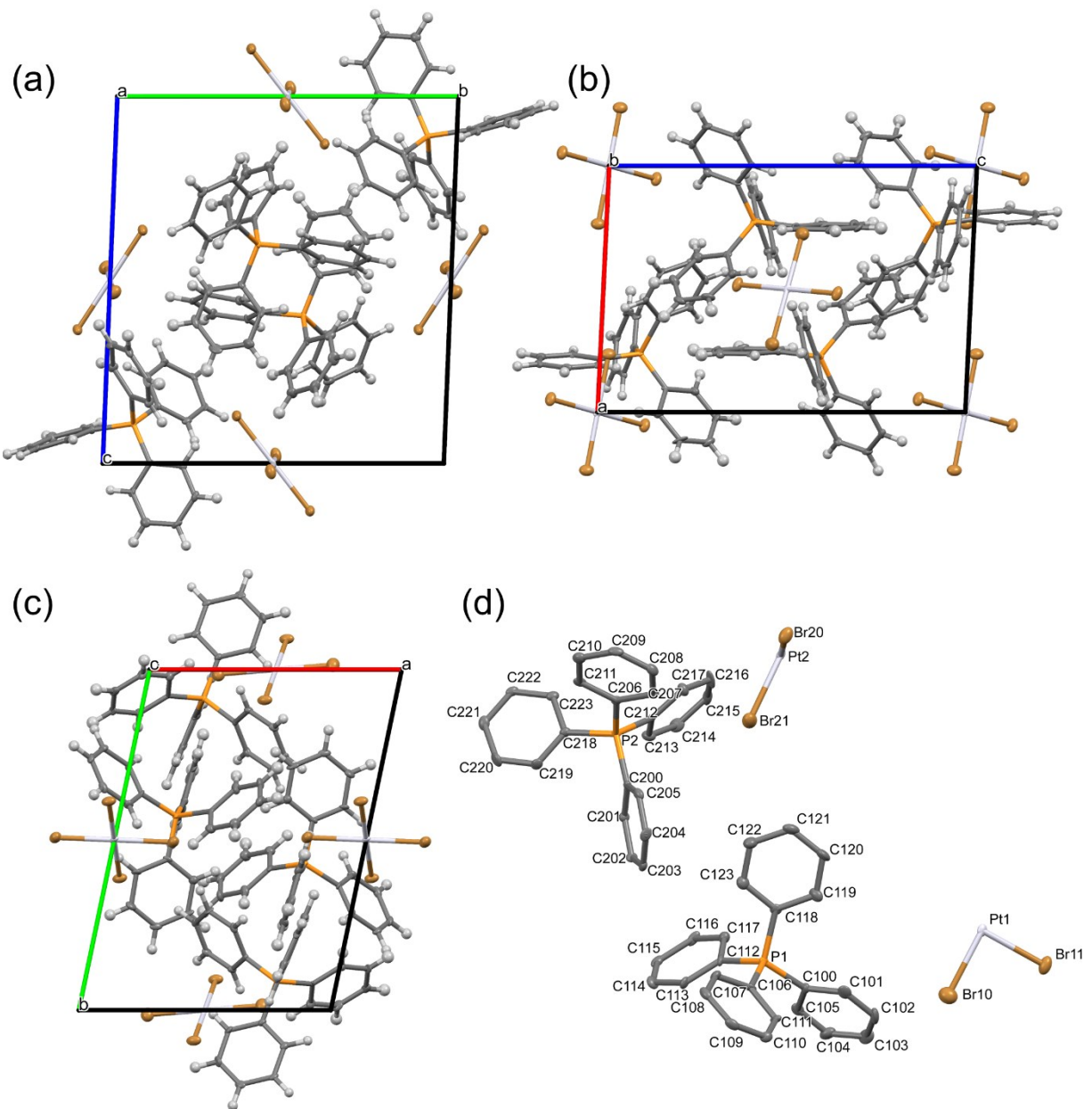


Figure S6. Crystal packing along the crystallographic period a (a), b (b) and c (c) and asymmetric unit (d) of  $(\text{PPh}_4)_2[\text{PtBr}_4]$  salt. Color code: Pt – pale grey, P – orange, Br – brown, C – dark grey, H – grey. Thermal ellipsoids are drawn at the 50% probability level. In (d) hydrogen atoms are omitted for clarity. The crystal structure of organic salt is composed of  $[\text{PPh}_4]^+$  cations and  $[\text{PtBr}_4]^{2-}$  anionic complexes. The asymmetric unit contains 2 halves of  $[\text{PtBr}_4]^{2-}$  and 2  $[\text{PPh}_4]^+$  moieties. In contrast to its analogs ( $[\text{Pt}(\text{CN})_4]^{2-}$ ,  $\text{S}^1$  and  $[\text{PtCl}_4]^{2-}$ ,  $\text{S}^2$ ),  $(\text{PPh}_4)_2[\text{PtBr}_4]$  crystallizes in triclinic crystal system (see Table S3).

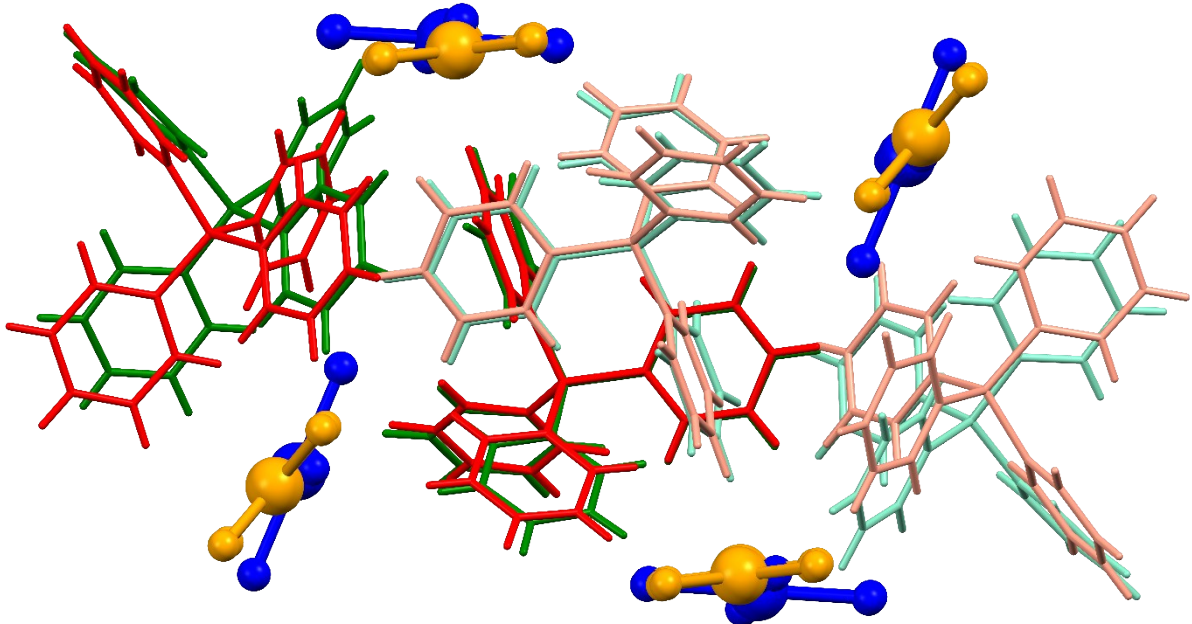


Figure S7. Comparison of crystal packing between  $(\text{PPh}_4)_2[\text{PtBr}_4]$ ,<sup>(this paper)</sup> (cold color palette) and  $(\text{PPh}_4)_2[\text{PtCl}_4]$ ,<sup>S2</sup> (warm color palette) salts. Color code: blue –  $[\text{PtBr}_4]^{2-}$ , light green – front cations, green – rear cations, orange –  $[\text{PtCl}_4]^{2-}$ , light red – front cations, red – rear cations. Despite different space groups and even crystal systems, both salts show almost identical supramolecular topology. The molecules possess slightly different arrangements.

Table S3. Crystal data and structure refinement for  $[\text{PPh}_4]^+$  salts of  $[\text{PtBr}_4]^{2-}$ ,  $[\text{PtCl}_4]^{2-\text{S}2}$ , and  $[\text{Pt}(\text{CN})_4]^{2-\text{S}1}$ .

Identification code	<b>PtBr<sub>4</sub></b>	<b>PtCl<sub>4</sub> (VAZBIK)</b>	<b>Pt(CN)<sub>4</sub> (TUNCEN)</b>
Reference	This paper	2	1
Empirical formula	C <sub>48</sub> H <sub>40</sub> Br <sub>4</sub> P <sub>2</sub> Pt	C <sub>48</sub> H <sub>40</sub> Cl <sub>4</sub> P <sub>2</sub> Pt	C <sub>52</sub> H <sub>42</sub> N <sub>4</sub> OP <sub>2</sub> Pt
Crystal system	<b>triclinic</b>	<b>monoclinic</b>	<b>monoclinic</b>
Space group	<b>P-1</b>	<b>P2<sub>1</sub>/n</b>	<b>P2<sub>1</sub>/n</b>
a/Å	<b>10.165(6)</b>	<b>10.3287</b>	<b>10.4893</b>
b/Å	<b>14.041(9)</b>	<b>15.8891</b>	<b>15.9398</b>
c/Å	<b>14.832(8)</b>	<b>12.9799</b>	<b>12.9612</b>
$\alpha/^\circ$	<b>91.767(18)</b>	<b>90</b>	<b>90</b>
$\beta/^\circ$	<b>92.28(2)</b>	<b>95.077</b>	<b>94.7400</b>
$\gamma/^\circ$	<b>101.670(14)</b>	<b>90</b>	<b>90</b>
Volume/Å <sup>3</sup>	<b>2070(2)</b>	<b>2121.82</b>	<b>2159.67</b>
Z	2	2	2
Formula weight	1193.47	-	995.92
Temperature/K	100.0	100.0	100.0
$\rho_{\text{calc}}/\text{cm}^3$	1.915	-	-
$\mu/\text{mm}^{-1}$	7.362	-	-
F(000)	1152.0	-	-
Crystal size/mm <sup>3</sup>	0.45 × 0.44 × 0.38	-	-
Radiation	MoK $\alpha$ ( $\lambda = 0.71073$ )	-	-
2 $\Theta$ range for data collection/°	4.826 to 50.364	-	-
Index ranges	-12 ≤ h ≤ 12 -16 ≤ k ≤ 16 -17 ≤ l ≤ 17	-	-
Reflections collected	16523	-	-
Independent reflections	7254 [R <sub>int</sub> = 0.0420, R <sub>sigma</sub> = 0.0551]	-	-
Data/restraints/parameters	7254/18/499	-	-
Goodness-of-fit on F <sup>2</sup>	1.046	-	-
Final R indexes [I>=2σ (I)]	R <sub>1</sub> = 0.0487 wR <sub>2</sub> = 0.1245	-	-
Final R indexes [all data]	R <sub>1</sub> = 0.0651 wR <sub>2</sub> = 0.1340	-	-
Largest diff. peak/hole / e Å <sup>-3</sup>	3.35/-2.53	-	-

## Spectroscopic characterization

### Electronic absorption spectroscopy

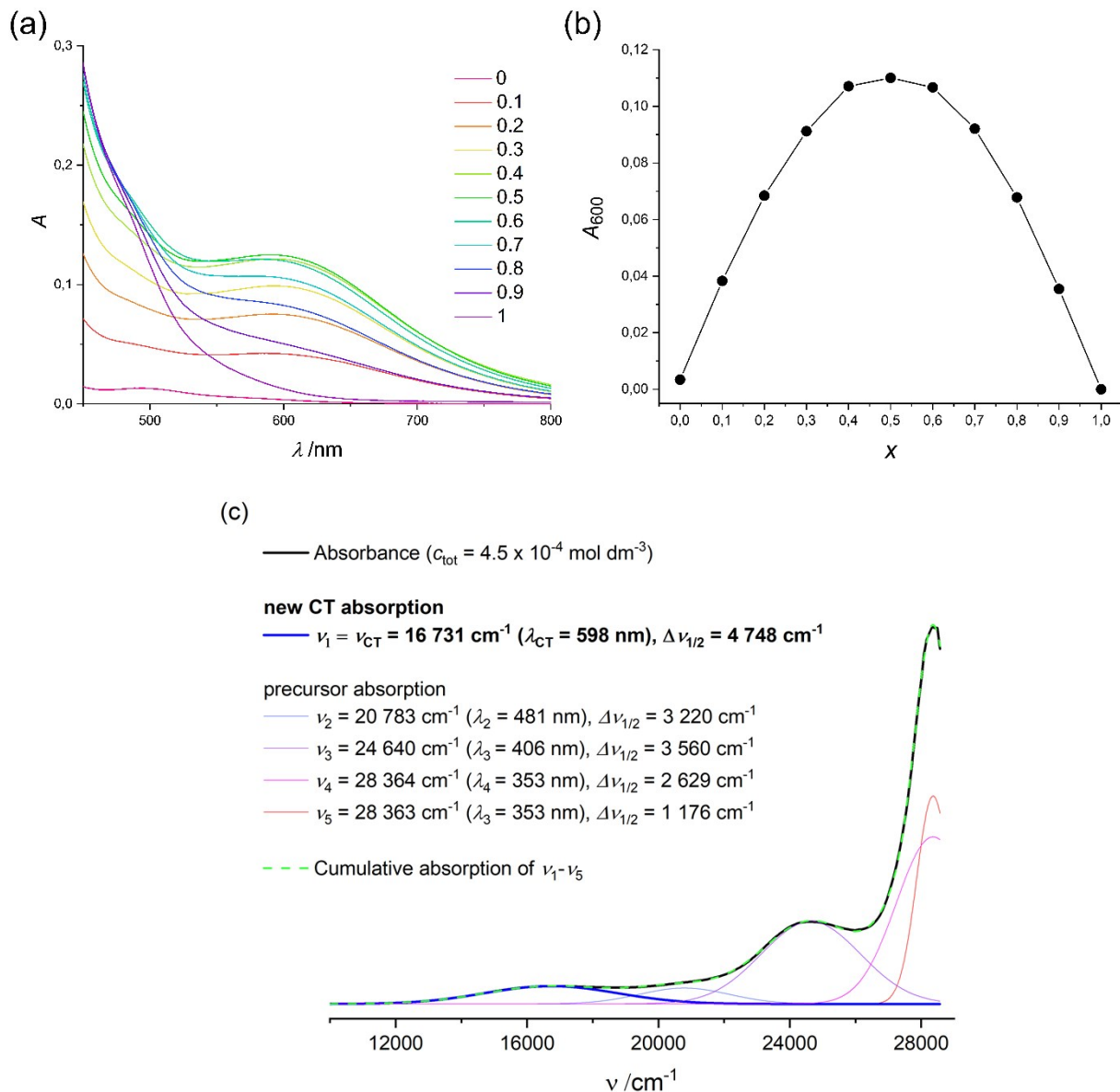


Figure S8. UV-Vis studies on  $\{[\text{PtCl}_4]^{2-}; \text{HAT}(\text{CN})_6\}$  adduct in MeCN solution. Top panel: determination of the molecular ratio 1:1 for the CT chromophore: (a) the spectra of the mixtures of  $(\text{PPh}_4)_2[\text{PtCl}_4]^{2-}$  and  $\text{HAT}(\text{CN})_6$  for different  $x = c_{\text{HAT}}/(c_{\text{HAT}} + c_{\text{Pt}})$  (the denominator has the constant value along the series) ( $T = 298 \text{ K}$ ); (b) the Job plot constructed based on the absorbance values at  $\lambda = 600 \text{ nm}$ ,  $A_{600}$ , after the appropriate correction with the absorbance of components (mainly  $\text{HAT}(\text{CN})_6$ ) (the solid line is for eye-guide only). The similar contour was obtained looking at the  $A_{650}$  and  $A_{700}$  series. Bottom panel: deconvolution of the absorption spectrum.

## Nuclear Magnetic Resonance $^{13}\text{C}$ experiments

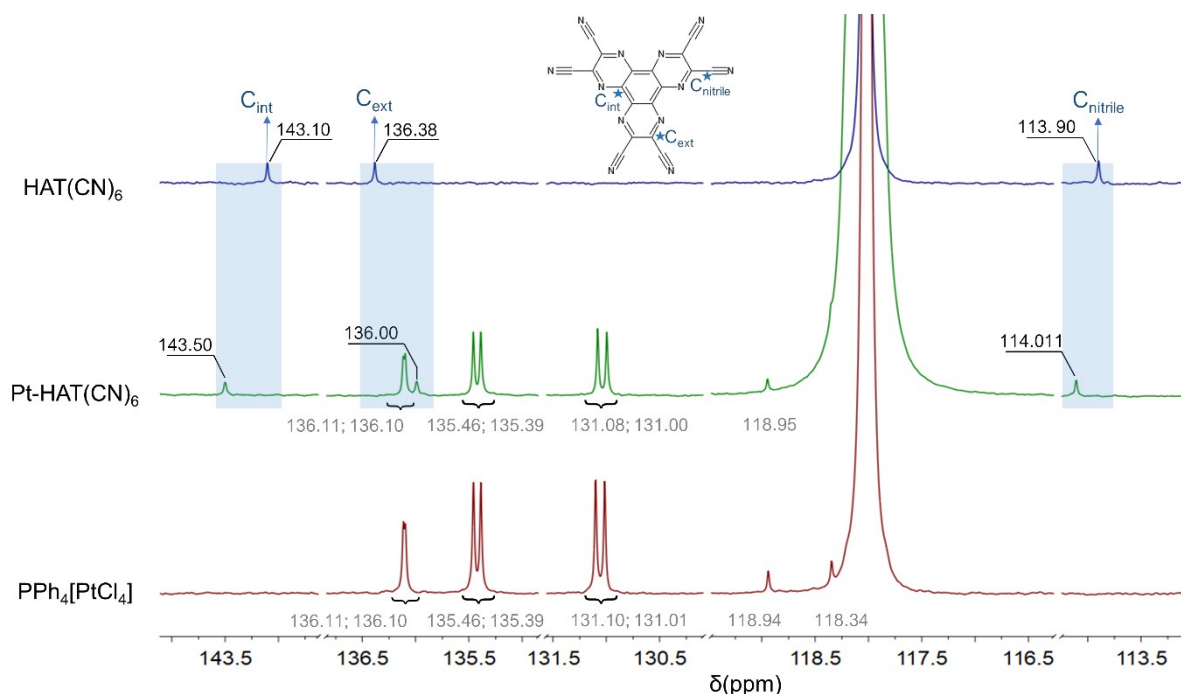


Figure S9.  $^{13}\text{C}$  NMR spectra of  $\text{HAT}(\text{CN})_6$  (blue),  $\{\text{PtCl}_4\} \cdot \text{HAT}(\text{CN})_6$  adduct (green) and  $(\text{PPh}_4)_2[\text{PtCl}_4]$  salt (red) in  $\text{CD}_3\text{CN}$  solution. Concentrations:  $\text{HAT}(\text{CN})_6 - 0.009 \text{ mol dm}^{-3}$ ,  $(\text{PPh}_4)_2[\text{PtCl}_4] - 0.013 \text{ mol dm}^{-3}$ , adduct –  $4.5 \times 10^{-4} \text{ mol dm}^{-3}$  ( $T = 298 \text{ K}$ ). All samples were prepared by dissolving solids in  $\text{CD}_3\text{CN}$ . Significant changes in chemical shifts of  $\text{HAT}(\text{CN})_6$  carbon atoms are marked by shaded regions.

Table S4.  $^{13}\text{C}$  NMR chemical shifts of  $\text{HAT}(\text{CN})_6$  carbon atoms in **1-Cl<sup>-</sup>** in comparison to **1-CN<sup>-</sup>** and pristine **HAT(CN)<sub>6</sub>**. Compare with Figure S9.

	$\delta$ (ppm)		
	<b>HAT(CN)<sub>6</sub></b>	<b>1-Cl<sup>-</sup></b>	<b>1-CN<sup>-</sup>,<sup>S1</sup></b>
$\text{C}_{\text{int}}$	143.10	143.50	143.33
$\text{C}_{\text{ext}}$	136.38	136.00	136.24
$\text{C}_{\text{nitrile}}$	113.90	114.01	114.02

## Quantum-chemical calculations

### Computational details

All calculations were performed using density functional theory (DFT)<sup>S3</sup> or its time-dependent variant (TD-DFT),<sup>S4</sup> following in general the computational protocol established in the previous studies on anion- $\pi$  supramolecular systems with polycyanidometalates and reported in References S1, S5, S6 and S7. The computations involved periodic and molecular cluster approaches and were carried out for both the novel  $[\text{PtBr}_4]^{2-}/\text{HAT}(\text{CN})_6$  ( $\text{X} = \text{Cl}, \text{Br}$ ) systems and for the previously reported  $[\text{Pt}(\text{CN})_4]^{2-}/\text{HAT}(\text{CN})_6$  assemblies.<sup>S1</sup> Note that Reference 1 presents some results of the computational analysis of the electronic structure of the latter compound; such analysis was repeated (and profoundly extended) here to ensure a direct comparison with the systems with the halogeno-complexes.

Periodic network calculations utilized the Vienna ab initio simulation package, version 5.4.4. (VASP 5.4.4.).<sup>S8</sup> In such computations, a plane-wave basis set was used with an energy cutoff of 400 eV, core electronic states were described by means of the projector augmented wave (PAW) method,<sup>S9</sup> and valence electronic shells were treated explicitly. The calculations involved: (i) the Perdew-Burke-Ernzerhof (PBE)<sup>S10</sup> density functional of gradient generalized approximation (GGA) type with the third-generation Grimme's set of semiempirical dispersion corrections D3<sup>S11</sup> (as implemented in VASP upon using IVDW = 12 tag)<sup>S12</sup> and a Hubbard correction potential (with U-J = 2) defined within GGA+U method framework without LSDA exchange splitting,<sup>S13</sup> referred to as PBE+D3+U, and (ii) the HSE06<sup>S14</sup> range-separated hybrid density functional. The results obtained with the latter functional were used to analyse densities of states for **1-Cl<sup>-</sup>**, **1-Br<sup>-</sup>** and **1-CN<sup>-</sup>**. Bader charges were calculated by partitioning the valence electronic charge density by means of a non-commercial script.<sup>S15</sup>

ETS-NOCV<sup>S16</sup> analysis was performed using the Amsterdam Density Functional program, version 2017.106 (ADF 2017.106),<sup>S17</sup> with PBE+D3 and Becke, 3-parameter, Lee-Yang-Parr (B3LYP)<sup>S18</sup> +D3 density functionals and the TZ2P basis set, as implemented in the ADF package. Relativistic effects were addressed via the scalar zeroth-order regular approximation (ZORA) formalism.<sup>S19</sup> These calculations were performed on molecular clusters of  $[\text{PtL}_4]^{2-}/\text{HAT}(\text{CN})_6/[\text{PtL}_4]^{2-}$  sandwich structure ( $\text{L} = \text{Cl}, \text{Br}, \text{CN}$ ), extracted from the optimized (PBE+D3+U) geometries of the crystals. For such clusters, HOMO-LUMO gap values were also calculated with the PBE, B3LYP, and HSE06 density functionals.

$[\text{PtL}_4]^{2-}/\text{HAT}(\text{CN})_6$  adducts of the 1:1 stoichiometry ( $\text{L} = \text{Cl}, \text{CN}$ ) were optimized using the Turbomole program, version 7.3 (TM7.3),<sup>S20</sup> and employing the Becke88-Perdew86 (BP86)<sup>S21</sup> GGA density functional and the SVP<sup>S22</sup> basis set along with a 60-electron scalar relativistic effective core potential (ECP) for platinum atom to take into account relativistic effects.<sup>S23</sup> Conductor-like screening model (COSMO)<sup>S24,S25</sup> method was used here to model effects of the acetonitrile solvent by representing it as a continuum medium defined by its dielectric constant ( $\epsilon = 35.688$ ). The UV-Vis absorption (covering the 100 lowest singlet excitation energies along with the associated dipole strengths) was computed using the Gaussian program, version 16.C.01 (G16.C.01),<sup>S26</sup> with the Coulomb-attenuated method B3LYP (CAM-B3LYP)<sup>S27</sup> density functional, the TZVPS<sup>S21</sup> basis set along the corresponding ECP for Pt, and incorporating polarizable continuum model (PCM)<sup>S24,S28</sup> to account for a presence of acetonitrile solvent. The corresponding UV-Vis spectra were generated utilizing the GaussView 5.0.9<sup>S29</sup> graphical user interface, as the sums of Gaussian functions centred at the vertical singlet excitation energies and scaled using the calculated oscillator strengths with the default value (0.333 eV) of the implemented half-width at half-height (HWHH) parameter.

## Additional calculated results

Table S5. HOMO (HO) and LUMO (LU) orbital energies along with the corresponding HOMO-LUMO gaps (all values in eV) calculated for the  $[\text{PtL}_4]^{2-}/\text{HAT}(\text{CN})_6/[\text{PtL}_4]^{2-}$  molecular clusters extracted from the optimized coordinates of **1-Cl<sup>-</sup>**, **1-Br<sup>-</sup>** and **1-CN<sup>-</sup>**.

	PBE			B3LYP			HSE06 ( $\omega=0.11$ ) <sup>a</sup>			HSE06 ( $\omega=0.2$ ) <sup>a</sup>		
gas-phase												
L	HO	LU	gap	HO	LU	gap	HO	LU	gap	HO	LU	gap
Cl	4.75	5.05	0.29	4.07	5.43	1.36	4.12	5.10	0.98	4.29	5.00	0.71
Br	4.49	4.90	0.41	3.74	5.29	1.54	3.80	4.97	1.17	3.98	4.87	0.89
CN	2.99	4.22	1.23	2.07	4.79	2.72	2.12	4.48	2.36	2.36	4.34	1.98
acetonitrile												
L	HO	LU	gap	HO	LU	gap	HO	LU	gap	HO	LU	gap
Cl	-4.71	-4.05	0.66	-5.66	-3.50	2.15	-5.66	-3.86	1.80	-5.41	-3.99	1.42
Br	-4.70	-3.98	0.72	-5.58	-3.47	2.11	-5.58	-3.83	1.75	-5.34	-3.95	1.39
CN	-6.17	-4.40	1.77	-7.14	-3.77	3.37	-7.11	-4.11	3.00	-6.87	-4.26	2.61

<sup>a</sup> Note that for the HSE06 short range-separated hybrid functional two values of the range-separation (switching) parameter  $\omega$  was examined here, with the value of 0.11 / 0.2 corresponding to the standard / VASP functional parametrization.

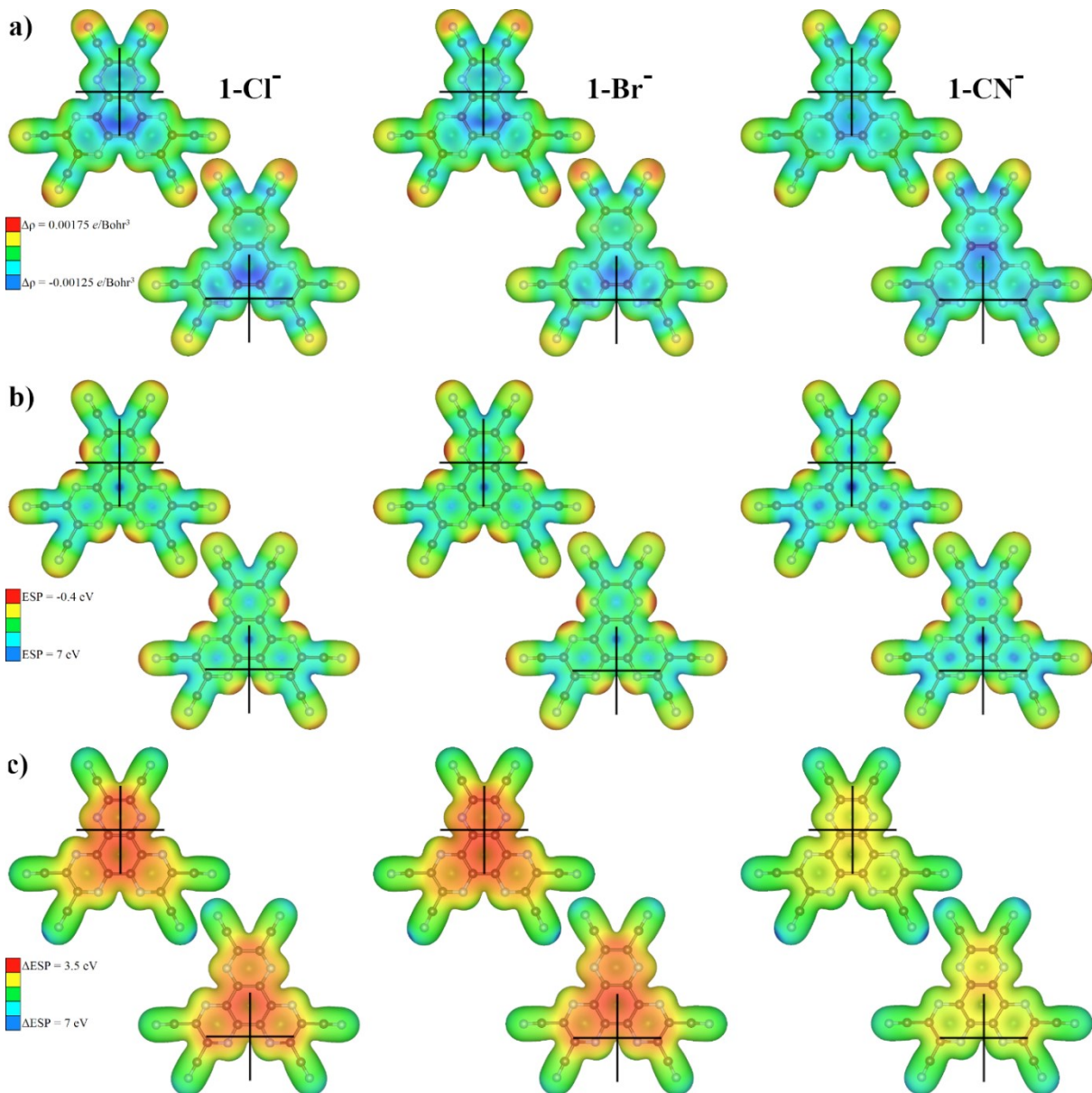


Figure S10. Electronic properties of HAT(CN)<sub>6</sub> computed with periodic network models for **1-Cl<sup>-</sup>**, **1-Br<sup>-</sup>** and **1-CN<sup>-</sup>**: a) Plots of  $\Delta\rho$  mapped onto the isosurface (0.02 au) of the electron density of a single HAT(CN)<sub>6</sub> molecule. Red / blue regions correspond to an inflow / outflow of electron density. b) Electrostatic potential (ESP) mapped onto the isosurface (0.02 au) of the electron density for HAT(CN)<sub>6</sub>. Red / blue color indicates electron-rich / electron-deficient area. c) Plots of  $\Delta\text{ESP}$  mapped onto the isosurface (0.02 au) of the electron density for HAT(CN)<sub>6</sub>. In all panels both ‘sides’ of HAT(CN)<sub>6</sub> molecule are shown with the location of the adjacent metal complex marked with the black cross.

Table S6. Values of total interaction energy between platinum complexes and HAT(CN)<sub>6</sub> along with its components as obtained from the ETS-NOCV analysis performed with PBE+D3 and B3LYP+D3 for the [PtL<sub>4</sub>]<sup>2-</sup>/HAT(CN)<sub>6</sub>/[PtL<sub>4</sub>]<sup>2-</sup> molecular clusters extracted from **1-Cl<sup>-</sup>**, **1-Br<sup>-</sup>** and **1-CN<sup>-</sup>**. Energies listed correspond to:  $\Delta E_{\text{int}}$  – total interaction,  $\Delta E_{\text{steric}}$  – steric interaction (representing a sum of  $\Delta E_{\text{elstat}}$  – electrostatic interaction and  $\Delta E_{\text{Pauli}}$  – Pauli repulsion),  $\Delta E_{\text{orb}}$  – orbital interaction, and  $\Delta E_{\text{disp}}$  – dispersion interaction.  $\Delta E_i$  and  $q_i$  ( $i = 1, 2, 3$ ) correspond to orbital interaction energy and charge measures for largest ETS-NOCV contributions to  $\Delta \rho$ . All energies are in kcal/mol, charge, given in parentheses, is in  $e$ .

	$\Delta E_{\text{int}}$	$\Delta E_{\text{steric}}$	$\Delta E_{\text{elstat}}$	$\Delta E_{\text{Pauli}}$	$\Delta E_{\text{orb}}$	$\Delta E_{\text{disp}}$	$\Delta E_1 (q_1)$	$\Delta E_2 (q_2)$	$\Delta E_3 (q_3)$
<b>PBE+D3</b>									
<b>1-Cl<sup>-</sup></b>	-144.75	-48.58	-103.35	54.77	-72.17	-24.00	-13.81 (-0.776)	-10.03 (-0.688)	-7.97 (-0.444)
<b>1-Br<sup>-</sup></b>	-132.63	-33.55	-110.42	76.87	-71.42	-27.67	-12.57 (-0.733)	-9.41 (-0.664)	-8.81 (-0.509)
<b>1-CN<sup>-</sup></b>	-103.59	-40.76	-83.29	42.52	-38.88	-23.94	-4.62 (-0.361)	-3.24 (-0.280)	-3.29 (-0.244)
<b>B3LYP+D3</b>									
<b>1-Cl<sup>-</sup></b>	-143.24	-44.66	-106.85	62.19	-58.80	-39.77	-8.56 (-0.542)	-5.63 (-0.434)	-6.10 (-0.340)
<b>1-Br<sup>-</sup></b>	-134.08	-27.12	-114.28	87.16	-59.66	-47.30	-8.28 (-0.523)	-5.75 (-0.445)	-6.73 (-0.396)
<b>1-CN<sup>-</sup></b>	-109.79	-36.24	-86.64	50.60	-35.63	-37.92	-3.70 (-0.266)	-2.61 (-0.202)	-2.76 (-0.191)

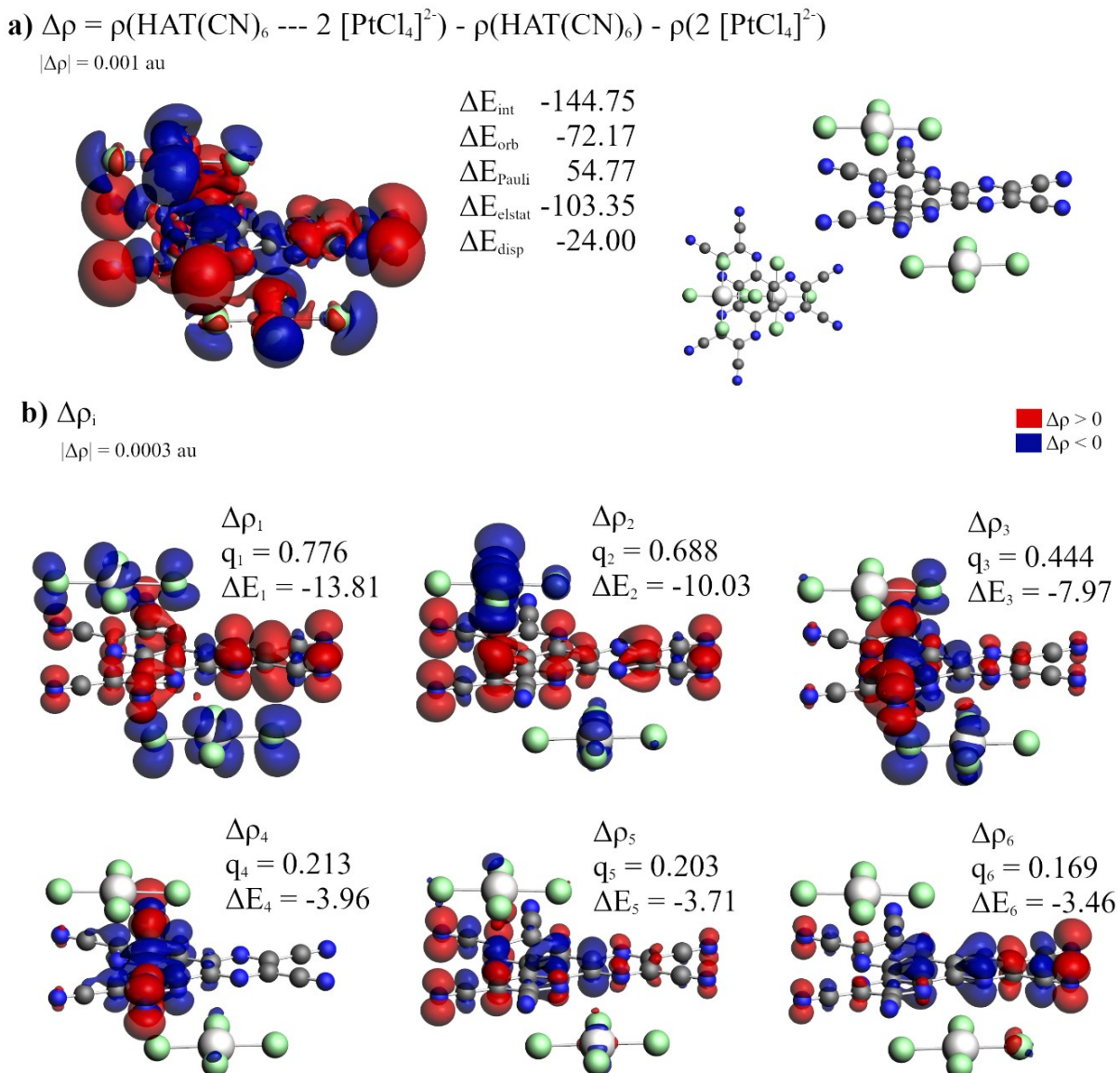


Figure S11. Results of ETS-NOCV analysis describing the interaction between  $[\text{PtCl}_4]^{2-}$ -complexes and  $\text{HAT}(\text{CN})_6$  in the molecular cluster extracted from the optimized (PBE+D3+U) crystal structure of **1-Cl<sup>-</sup>** (see panel a of the figure for a visualization of the cluster structure): a) Isosurface of differential electron density  $\Delta\rho$  ( $\pm 0.001 \text{ au}$ ) along with the energy values of  $\Delta E_{\text{int}}$  – total interaction,  $\Delta E_{\text{steric}}$  – steric interaction (representing a sum of  $\Delta E_{\text{elstat}}$  – electrostatic interaction and  $\Delta E_{\text{Pauli}}$  – Pauli repulsion),  $\Delta E_{\text{orb}}$  – orbital interaction, and  $\Delta E_{\text{disp}}$  – dispersion interaction. b) Isosurfaces of six dominant ETS-NOCV contributions to  $\Delta\rho$ , marked as  $\Delta\rho_n$  with  $n = 1-6$  ( $\pm 0.0003 \text{ au}$ ), along with the corresponding charge ( $q_n$ ) and orbital interaction energy ( $\Delta E_n$ ) measures (in  $e$  and kcal/mol, respectively). Red / blue color indicates gain / loss of electron density.

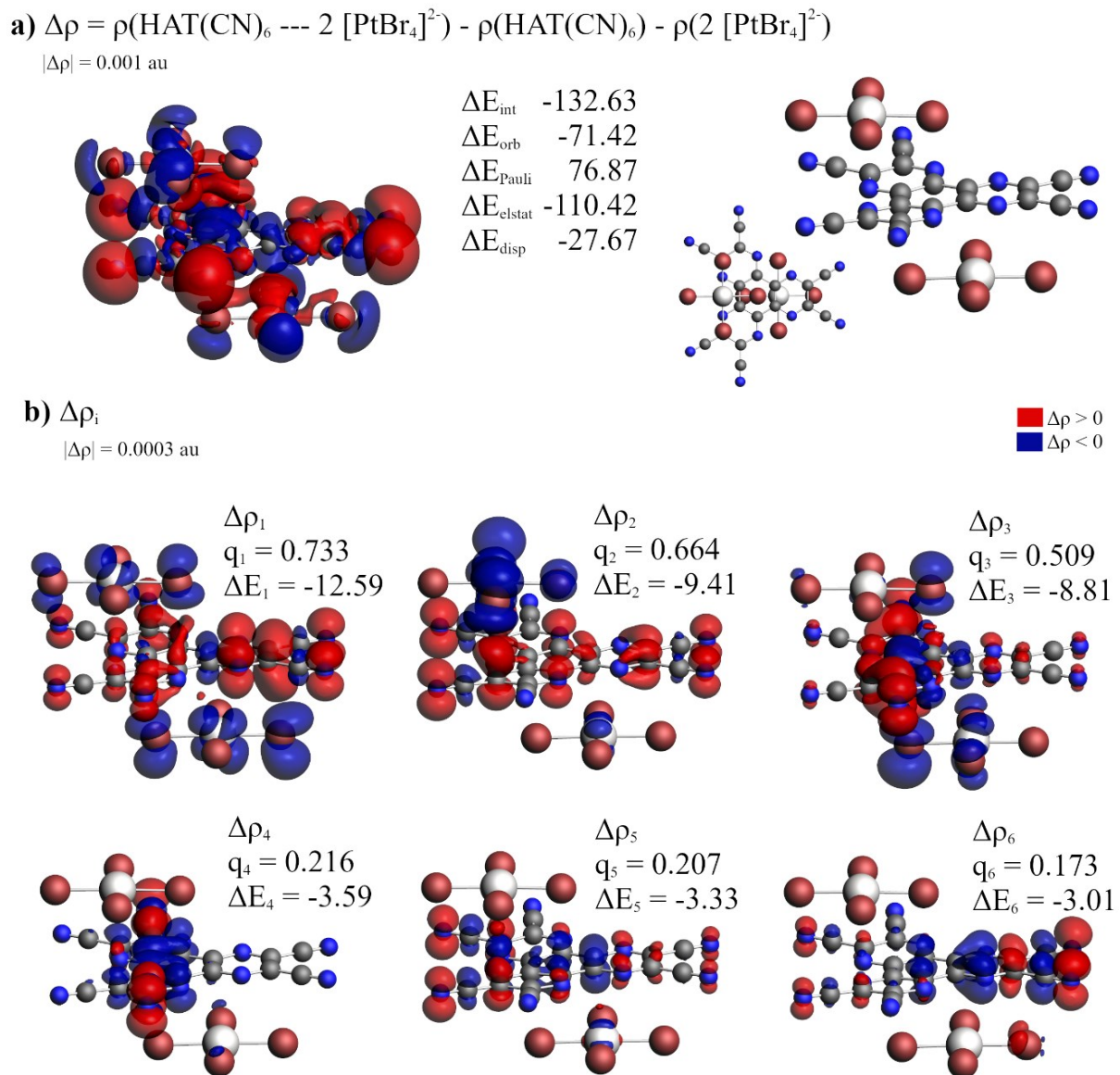
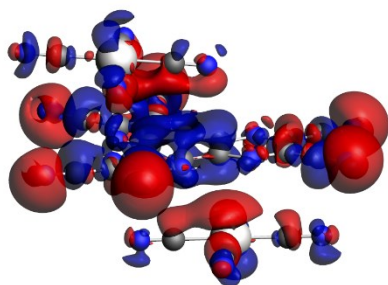


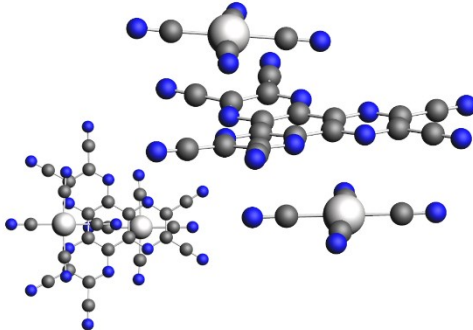
Figure S12. Results of ETS-NOCV analysis describing the interaction between  $[\text{PtBr}_4]^{2-}$  complexes and  $\text{HAT}(\text{CN})_6$  in the molecular cluster extracted from the optimized (PBE+D3+U) crystal structure of **1-Br** (see panel a of the figure for a visualization of the cluster structure): a) Isosurface of differential electron density  $\Delta\rho$  ( $\pm 0.001 \text{ au}$ ) along with the energy values of  $\Delta E_{\text{int}}$  – total interaction,  $\Delta E_{\text{steric}}$  – steric interaction (representing a sum of  $\Delta E_{\text{elstat}}$  – electrostatic interaction and  $\Delta E_{\text{Pauli}}$  – Pauli repulsion),  $\Delta E_{\text{orb}}$  – orbital interaction, and  $\Delta E_{\text{disp}}$  – dispersion interaction. b) Isosurfaces of six dominant ETS-NOCV contributions to  $\Delta\rho$ , marked as  $\Delta\rho_n$  with  $n = 1-6$  ( $\pm 0.0003 \text{ au}$ ), along with the corresponding charge ( $q_n$ ) and orbital interaction energy ( $\Delta E_n$ ) measures (in  $e$  and kcal/mol, respectively). Red / blue color indicates gain / loss of electron density.

a)  $\Delta\rho = \rho(\text{HAT}(\text{CN})_6 \cdots 2 [\text{Pt}(\text{CN})_4]^{2-}) - \rho(\text{HAT}(\text{CN})_6) - \rho(2 [\text{Pt}(\text{CN})_4]^{2-})$

$|\Delta\rho| = 0.001 \text{ au}$



$\Delta E_{\text{int}}$	-103.59
$\Delta E_{\text{orb}}$	-38.88
$\Delta E_{\text{Pauli}}$	42.52
$\Delta E_{\text{elstat}}$	-83.29
$\Delta E_{\text{disp}}$	-23.94



b)  $\Delta\rho_i$

$|\Delta\rho| = 0.0003 \text{ au}$

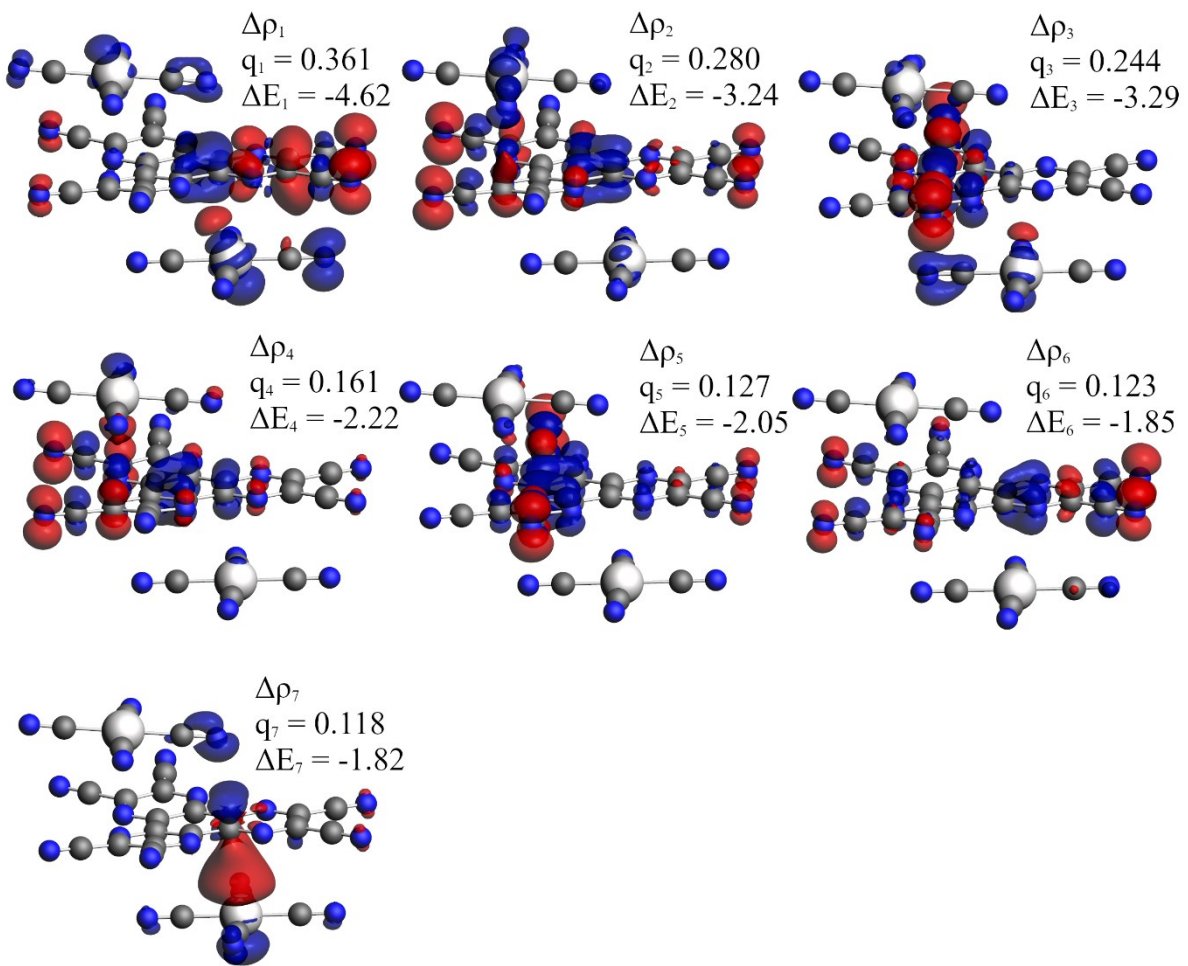


Figure S13. Results of ETS-NOCV analysis describing the interaction between  $[\text{Pt}(\text{CN})_4]^{2-}$  complexes and  $\text{HAT}(\text{CN})_6$  in the molecular cluster extracted from the optimized (PBE+D3+U) crystal structure of **1-CN** (see panel a of the figure for a visualization of the cluster structure): a) Isosurface of differential electron density  $\Delta\rho$  ( $\pm 0.001 \text{ au}$ ) along with the energy values of  $\Delta E_{\text{int}}$  – total interaction,  $\Delta E_{\text{steric}}$  – steric interaction (representing a sum of  $\Delta E_{\text{elstat}}$  – electrostatic interaction and  $\Delta E_{\text{Pauli}}$  – Pauli repulsion),  $\Delta E_{\text{orb}}$  – orbital interaction, and  $\Delta E_{\text{disp}}$  – dispersion interaction. b) Isosurfaces of seven dominant ETS-NOCV contributions to  $\Delta\rho$ , marked as  $\Delta\rho_n$  with  $n = 1-7$  ( $\pm 0.0003 \text{ au}$ ), along with the corresponding charge ( $q_n$ ) and orbital interaction energy ( $\Delta E_n$ ) measures (in  $e$  and kcal/mol, respectively). Red / blue color indicates gain / loss of electron density.

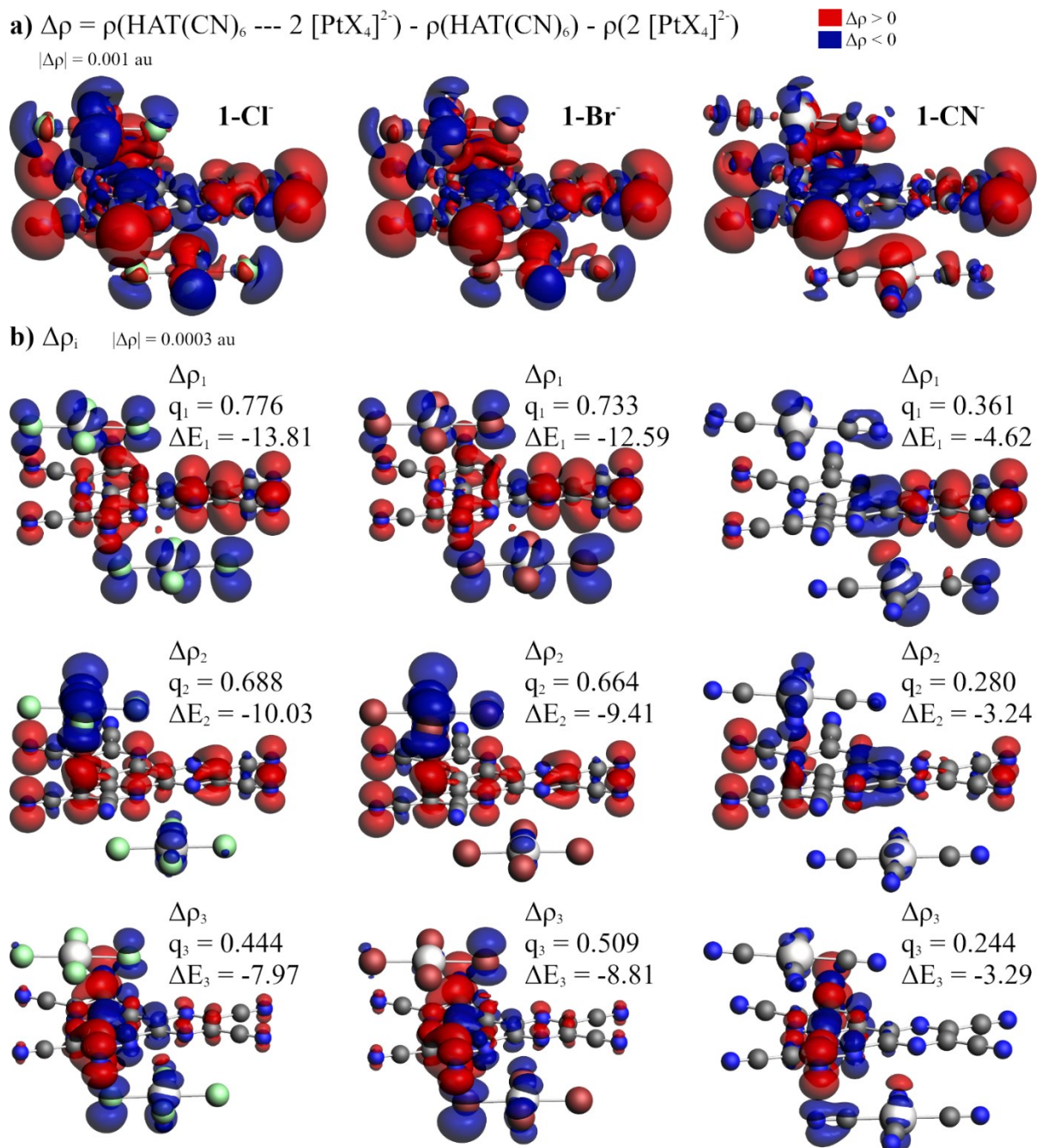


Figure S14. Comparison of the results of ETS-NOCV analysis describing the interaction between platinum complexes and  $\text{HAT}(\text{CN})_6$  in the molecular clusters extracted from the optimized (PBE+D3+U) crystal structures of **1-Cl<sup>-</sup>**, **1-Br<sup>-</sup>** and **1-CN<sup>-</sup>**: Isosurfaces of a) differential electron densities  $\Delta\rho$  ( $\pm 0.001 \text{ au}$ ) and b) three dominant ETS-NOCV contributions to  $\Delta\rho$ , marked as  $\Delta\rho_1$ ,  $\Delta\rho_2$  and  $\Delta\rho_3$  ( $\pm 0.0003 \text{ au}$ ), along with the corresponding charge ( $q_i$ ) and orbital interaction energy ( $\Delta E_i$ ) measures (in  $e$  and kcal/mol, respectively). Red / blue color indicates gain / loss of electron density.

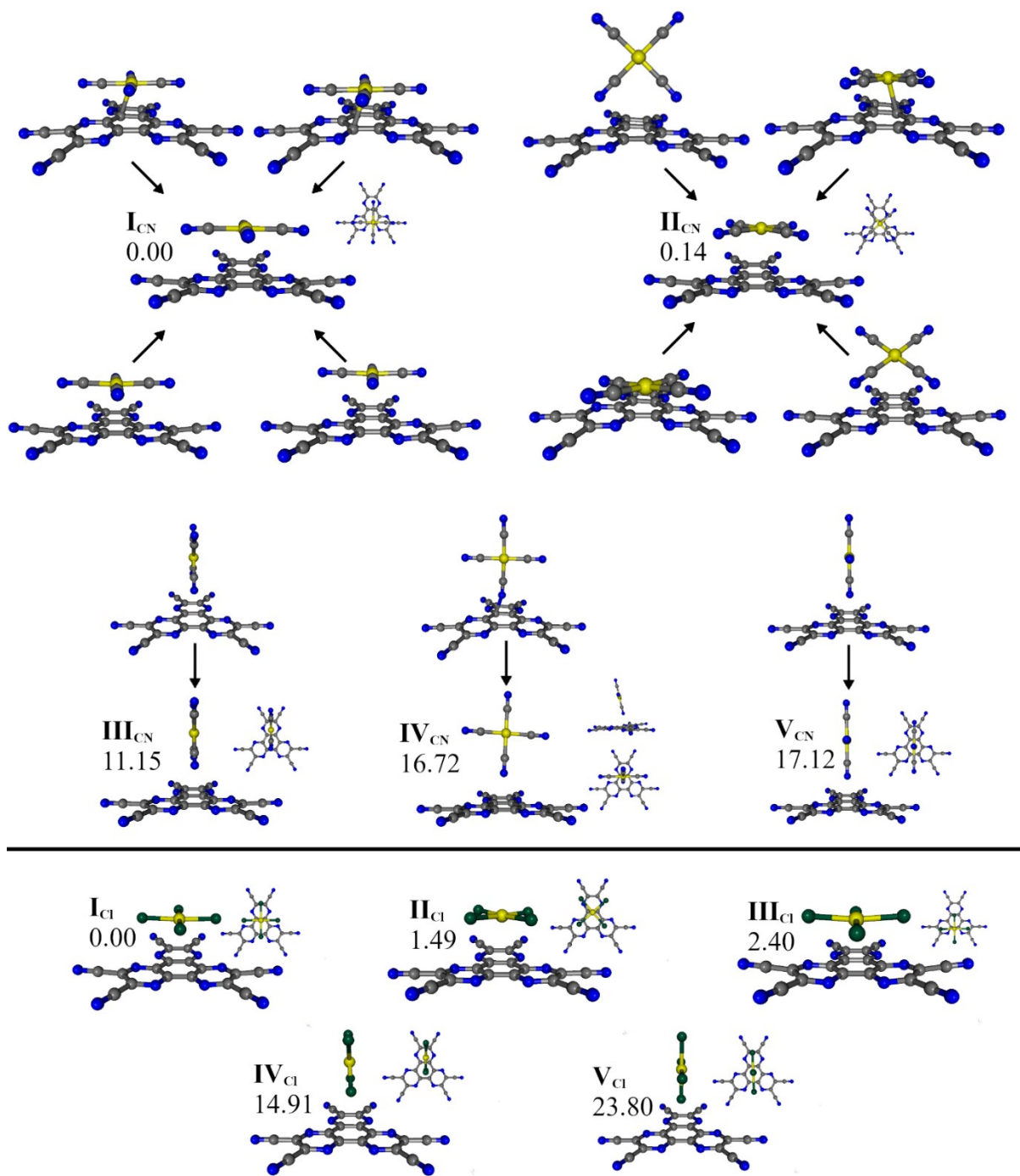


Figure S15. Optimized molecular structures computed for  $[\text{Pt}(\text{CN})_4]^{2-}/\text{HAT}(\text{CN})_6$  (top) and for  $[\text{PtCl}_4]^{2-}/\text{HAT}(\text{CN})_6$  (bottom) adducts of 1:1 stoichiometry with the corresponding energies calculated relative to the lowest-energy structure (in kcal/mol). For  $[\text{Pt}(\text{CN})_4]^{2-}/\text{HAT}(\text{CN})_6$  a full set of starting geometries is also shown, the analogous set was used in the conformation analysis for  $[\text{PtCl}_4]^{2-}/\text{HAT}(\text{CN})_6$ .

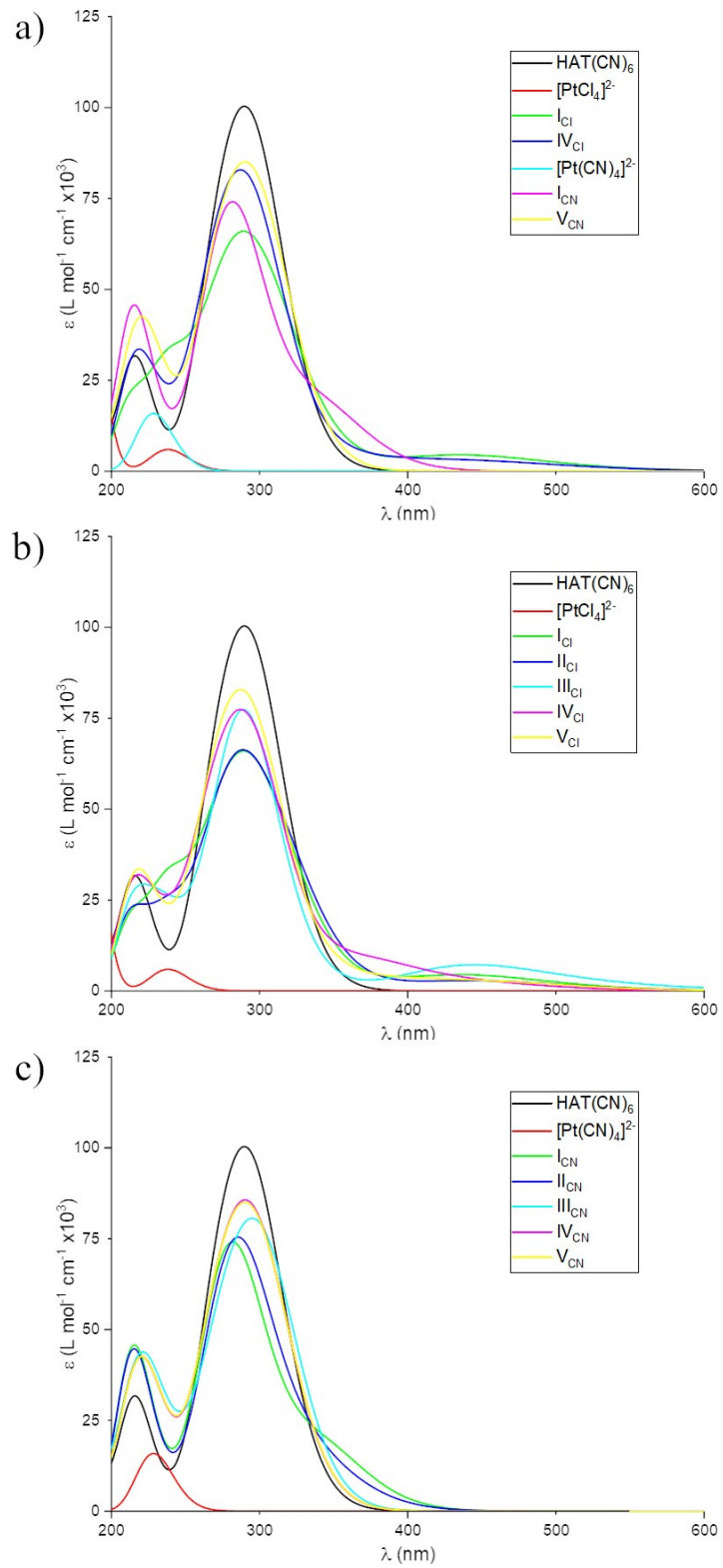


Figure S16. Simulated (TD-DFT CAM-B3LYP/TZVP/PCM(acetonitrile)) UV-Vis spectra for  $\text{Pt}(\text{CN})_4^{2-}/\text{HAT}(\text{CN})_6$  and  $[\text{PtCl}_4]^{2-}/\text{HAT}(\text{CN})_6$  adducts of 1:1 stoichiometry as shown Figure S15 and for their respective parent metal complexes and the pristine  $\text{HAT}(\text{CN})_6$  molecule. In b) and c) spectra computed for all optimized structures of  $[\text{PtCl}_4]^{2-}/\text{HAT}(\text{CN})_6$  and of  $\text{Pt}(\text{CN})_4^{2-}/\text{HAT}(\text{CN})_6$  are shown, while in a) a comparison between spectra obtained for representative  $[\text{PtCl}_4]^{2-}/\text{HAT}(\text{CN})_6$  and  $\text{Pt}(\text{CN})_4^{2-}/\text{HAT}(\text{CN})_6$  structures with the parallel and perpendicular arrangement of the metal complex and  $\text{HAT}(\text{CN})_6$  is presented.

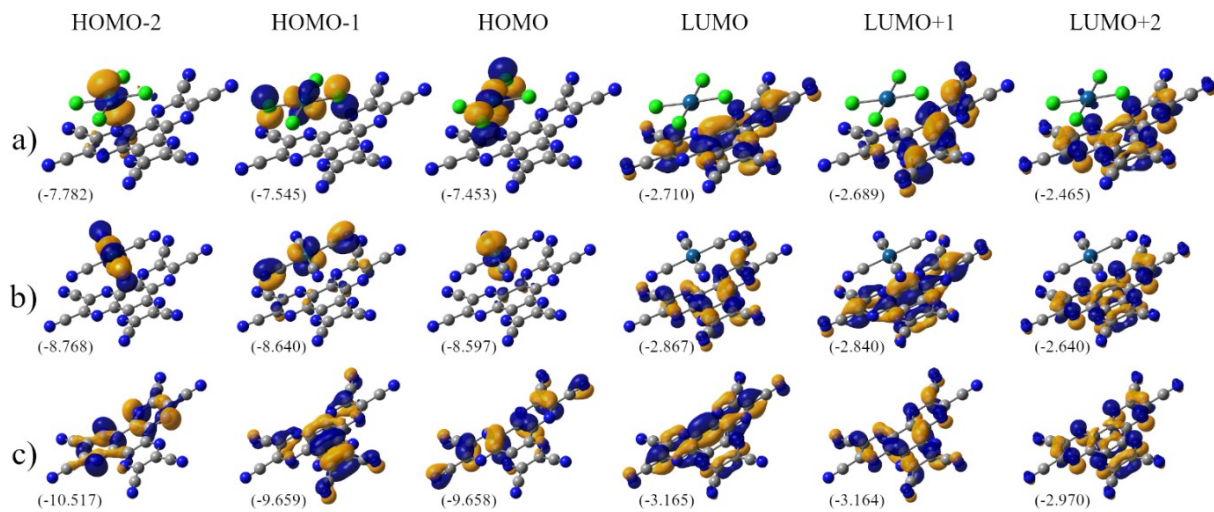


Figure S17. Isosurfaces ( $\pm 0.04$  au) of the frontier molecular orbitals for the structure a)  $\mathbf{I}_{\text{Cl}}$  of the  $[\text{PtCl}_4]^{2-}/\text{HAT}(\text{CN})_6$  system and b)  $\mathbf{I}_{\text{CN}}$  of the  $[\text{Pt}(\text{CN})_4]^{2-}/\text{HAT}(\text{CN})_6$  system (see Figure S15), and for c) the pristine  $\text{HAT}(\text{CN})_6$  molecule. The corresponding orbital energies (in eV) are listed in the parentheses. Orbitals presented in a) and b) are involved in electronic transitions that are responsible for appearance of additional low-energy intensities visible in the UV-Vis spectra shown in Figure S16.

## Crystalline composites characterization

**X-ray diffraction experiments, scanning electron microscopy (SEM) /energy dispersive X-ray spectroscopy (EDS)**

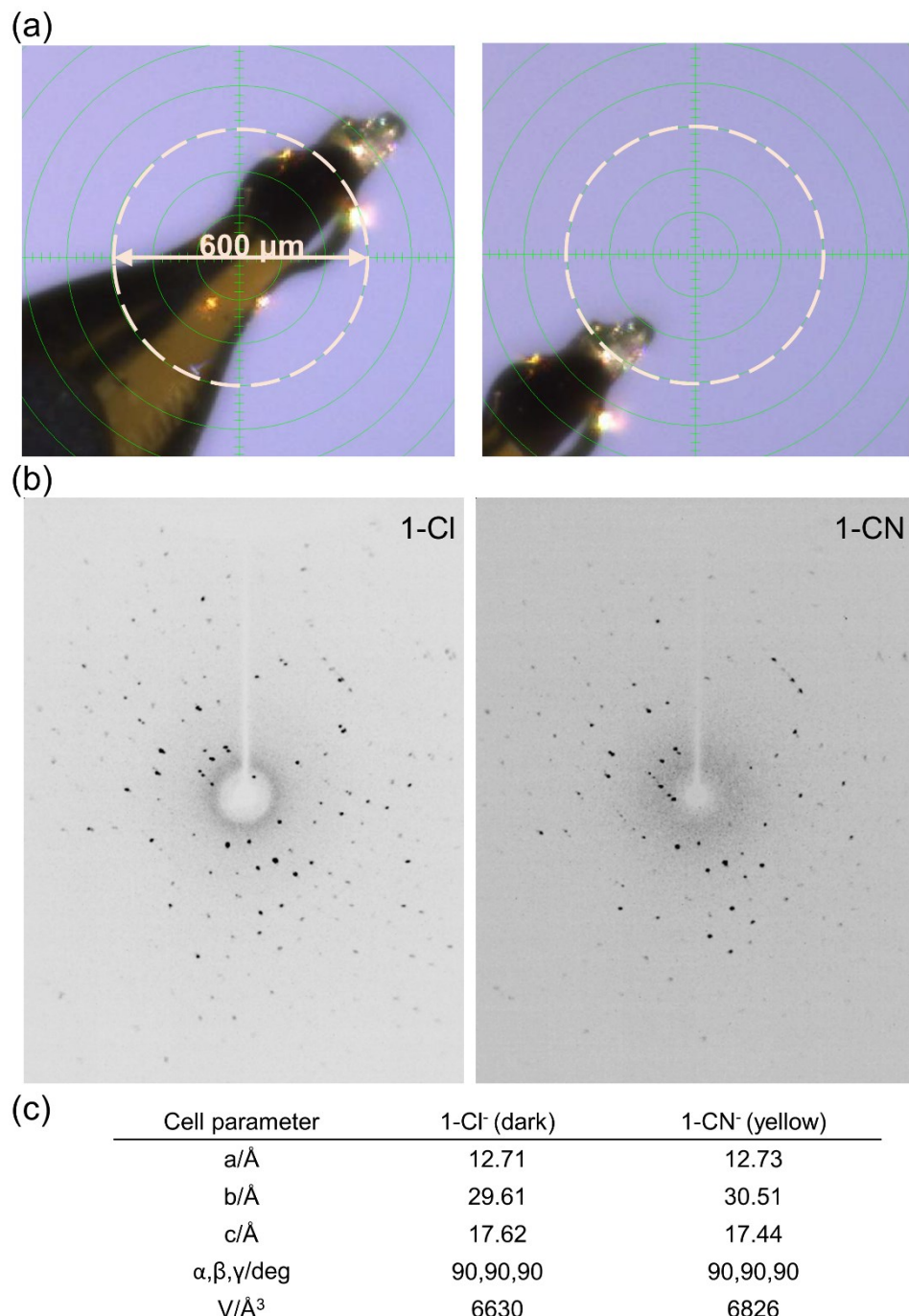


Figure S18. SC XRD measurement for the representative **1-Cl@1-CN** crystalline composite. (a) The X-ray beam focusing on the **1-Cl<sup>-</sup>** (seed, core, dark color) part (left) and on the **1-CN<sup>-</sup>** (shell, yellow color) part (right). (b) The representative diffraction frames. (c) The corresponding crystallographic cell parameters. Compare with those for the pristine crystals in Table S1.

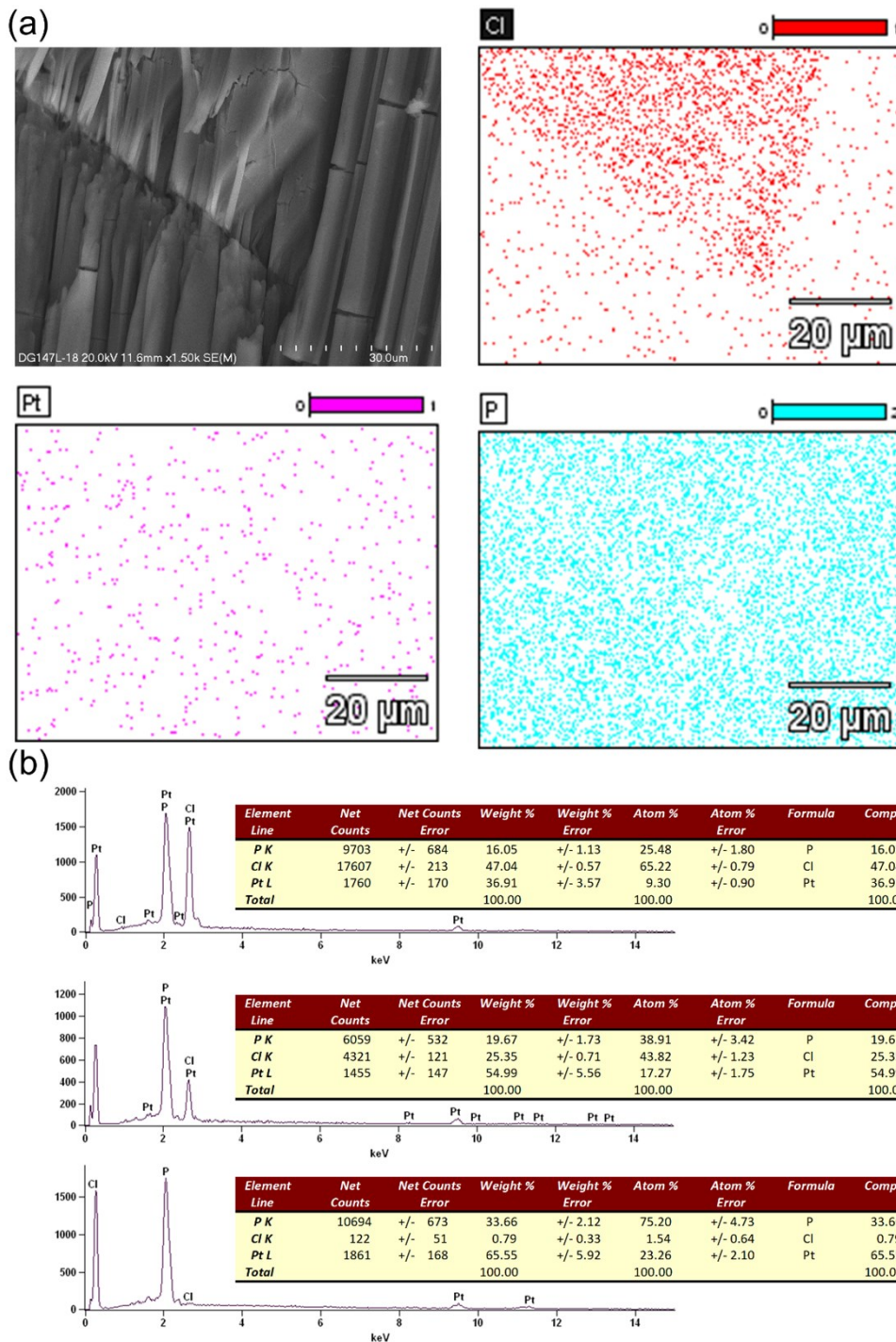
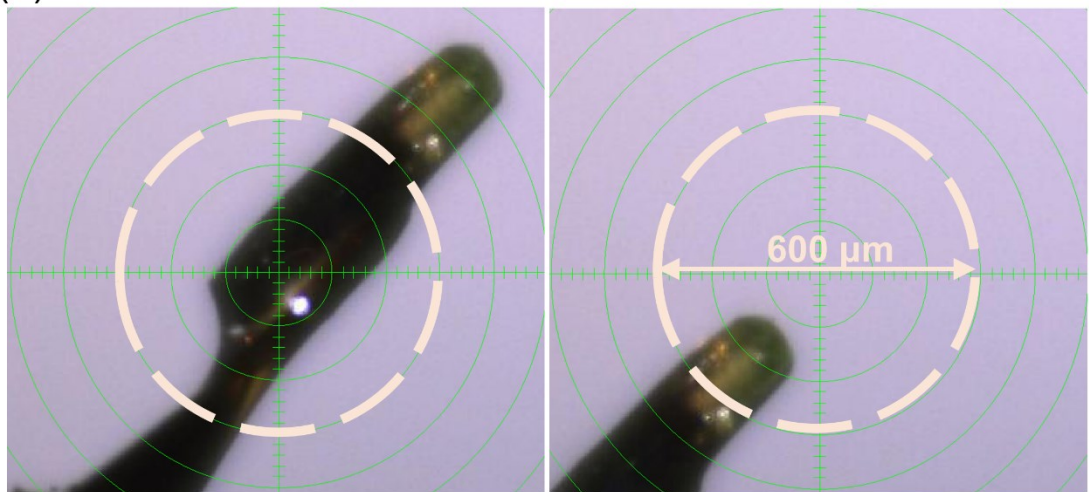
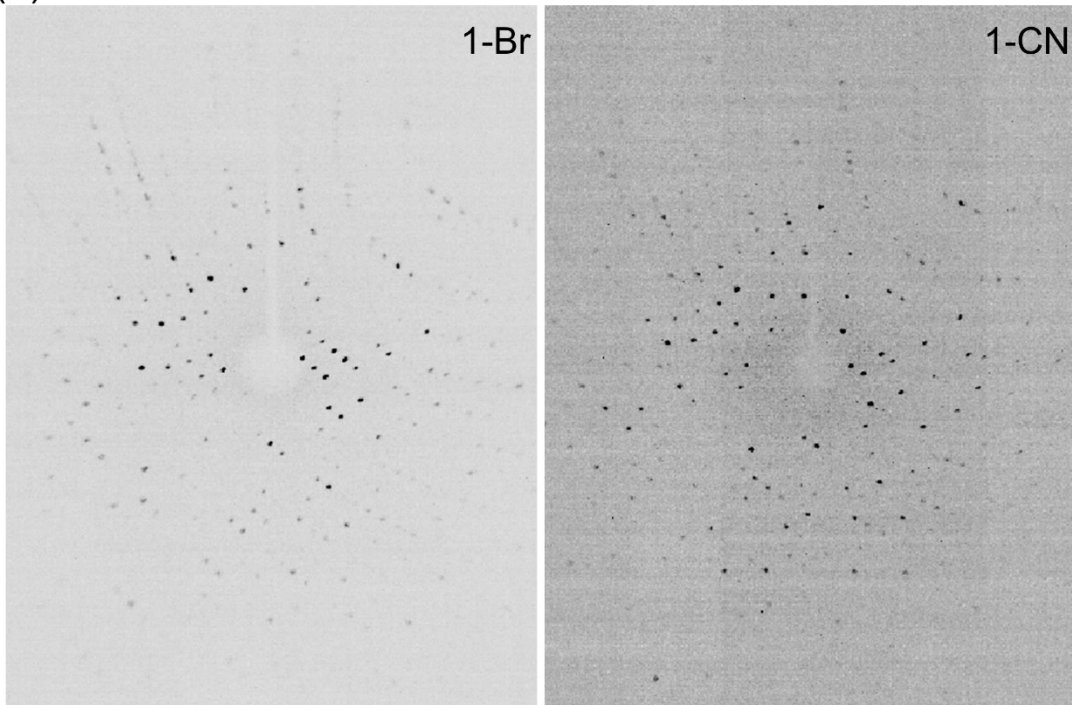


Figure S19. Representative results of SEM/EDS analysis for the **1-Cl@1-CN** composite. (a) The SEM image (magnification of 1500 x) of **1-Cl@1-CN** in the vicinity of the interface (appearing as the cracking line due to the fragility of this particular composite) together with SEM/EDS elemental Cl (red dots), Pt (magenta dots) and P (blue dots) mapping. The significant density of Cl in the upper part indicates the presence of  $[PtCl_4]^{2-}$  in the composite (**1-Cl<sup>-</sup>**), whereas the negligible amount of Cl in the lower part is in agreement with the presence of  $[Pt(CN)_4]^{2-}$  in the composite (**1-CN<sup>-</sup>**). (b) Representative EDS spectra collected from the phase **1-Cl<sup>-</sup>** (top), from the interface (middle) and from the phase **1-CN<sup>-</sup>** (bottom).

(a)



(b)



(c)

Cell parameter	1-Br <sup>-</sup> (dark)	1-CN <sup>-</sup> (yellow)
a/Å	12.75	12.75
b/Å	30.31	30.59
c/Å	17.54	17.50
$\alpha, \beta, \gamma/\text{deg}$	90,90,90	90,90,90
V/Å <sup>3</sup>	6778	6826

Figure S20. SC XRD measurement for the representative **1-Br@1-CN** crystalline composite. (a) The X-ray beam focusing on the **1-Br<sup>-</sup>** (seed, core, dark color) part (left) and on the **1-CN<sup>-</sup>** (shell, yellow color) part (right). (b) The representative diffraction frames. (c) The corresponding crystallographic cell parameters. Compare with those for the pristine crystals in Table S1.

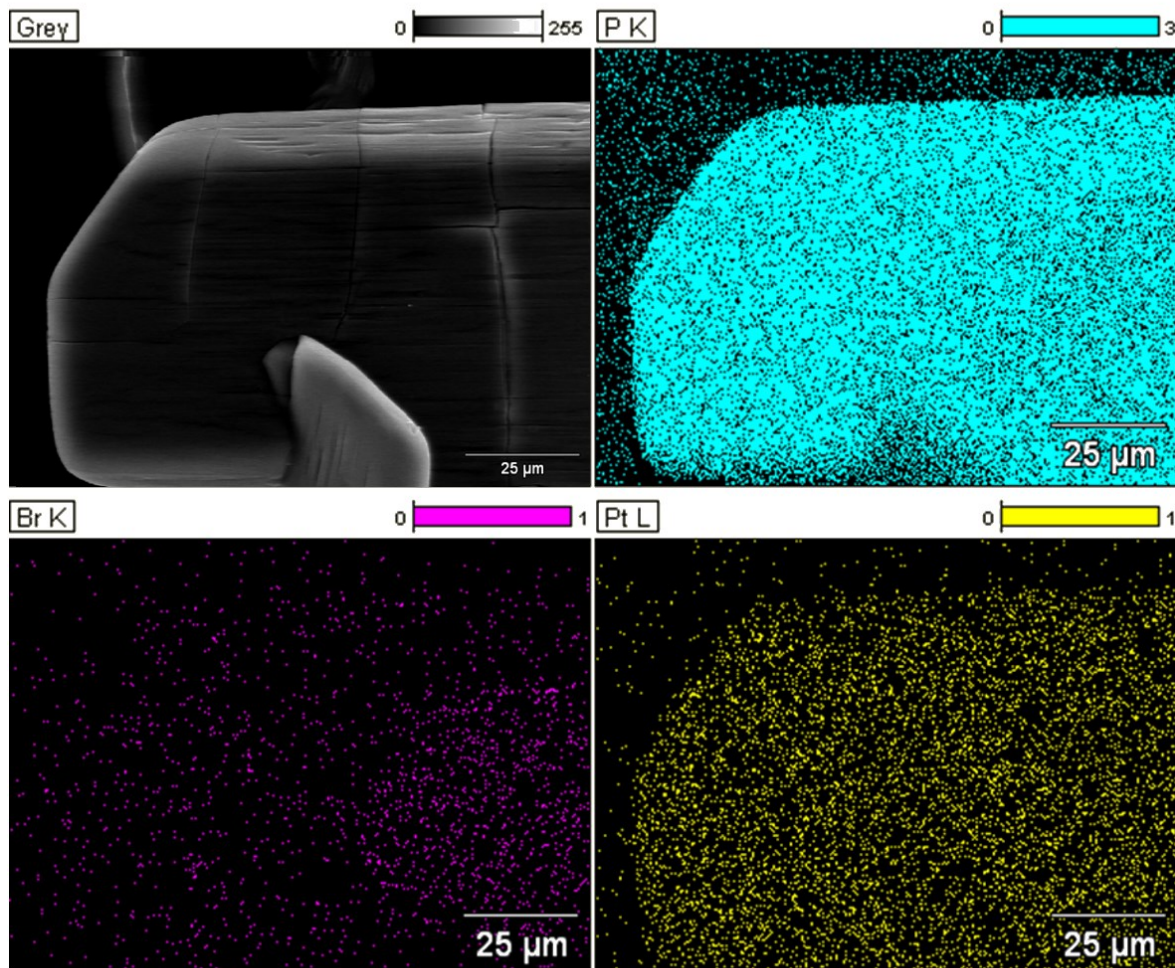


Figure S21. Representative results of SEM/EDS analysis for the **1-Br@1-CN** composite. The SEM image (magnification of 1500 x) of **1-Br@1-CN** in the vicinity of the interface together with SEM/EDS elemental Br (magenta dots), Pt (yellow dots) and P (cyan dots) mapping. The significant density of Br in the right part indicates the presence of  $[\text{PtBr}_4]^{2-}$  in the composite (**1-Br<sup>-</sup>**), whereas the negligible amount of Br in the left part is in agreement with the presence of  $[\text{Pt}(\text{CN})_4]^{2-}$  in the composite (**1-CN<sup>-</sup>**).

## FT IR characterization

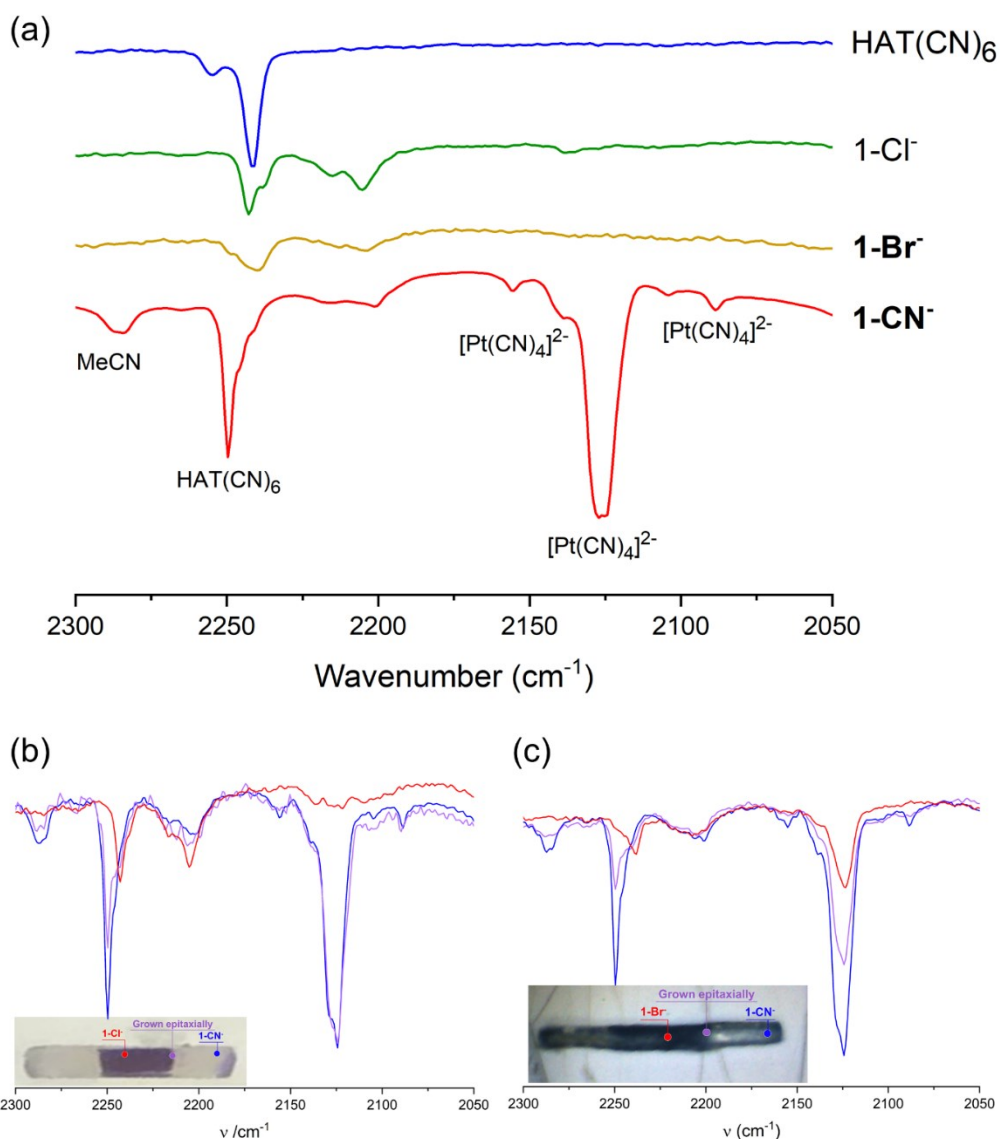


Figure S22. IR spectra for HAT(CN)<sub>6</sub>, **1-Cl<sup>-</sup>**, **1-Br<sup>-</sup>** and **1-CN<sup>-</sup>** (a), composites **1-Cl@1-CN** (b), and **1-Br@1CN** (c) in range of the stretching  $\nu(\text{C}\equiv\text{N})$  vibrations.

## Mixed **1**-Cl<sup>-</sup>/1-CN<sup>-</sup> crystals – DFT predictions

The comparable lattice parameters of **1**-CN<sup>-</sup> and **1**-Cl<sup>-</sup> suggest that they may, to some extent, be coaxed to co-exist within a common crystal lattice, although it must be cautioned that the *b* lattice parameter does vary substantially (up to 3%) and the higher CT character of the **1**-Cl<sup>-</sup> anion- $\pi$  interaction leads to a much increased binding energy of its anion- $\pi$  adducts in solution. As an exploration of the potential thermodynamic stability and electronic properties of mixed solid solution crystals, DFT-GGA calculations were run on analog structures of **1** that contain both [PtCN<sub>4</sub>]<sup>2-</sup> and [PtCl<sub>4</sub>]<sup>2-</sup> complexes, denoted as **1**-[(1-x)CN<sup>-</sup>][(x)Cl<sup>-</sup>] in Table S7. The computed DFT energies indicate that all of the mixed composite structures are less energetically stable than the parent single-complex structures, but the small magnitude of the reaction energies (always less than 0.1 eV per substituted complex) suggests that the complexes ‘fit’ into each other’s lattice fairly well. The computed band gap of the crystals are always comparable or less than the band gap of **1**-Cl<sup>-</sup>, which indicates that the frontier occupied molecular orbitals are localized on the [PtCl<sub>4</sub>]<sup>2-</sup> complexes.

Table S 7. Computed (PBE+D3+U) reaction energies, E<sub>rxn</sub>, of (1-x)**1**-CN<sup>-</sup> + (x)**1**-Cl<sup>-</sup> → **1**-[(1-x)CN<sup>-</sup>][(x)Cl<sup>-</sup>], where **1**-[(1-x)CN<sup>-</sup>][(x)Cl<sup>-</sup>] denotes a crystal structure that contains a 1-x fraction of [Pt(CN)<sub>4</sub>]<sup>2-</sup> complexes and an x fraction of [PtCl<sub>4</sub>]<sup>2-</sup> complexes (accordingly a structure with x = 0.00 / 1.00 corresponds to pure **1**-CN<sup>-</sup> / **1**-Cl<sup>-</sup>). Note that the simulation cell contains four metal complexes.

<i>x</i>	structure	E <sub>rxn</sub> / eV	E <sub>gap</sub> / eV
0.00	1	0.000	2.017
0.25	1	0.081	0.740
0.50	1	0.163	0.567
	2	0.122	0.865
0.75	1	0.050	0.753
1.00	1	0.000	0.893

## References

- S<sup>1</sup> E. Kuzniak, D. Pinkowicz, J. Hooper, M. Srebro-Hooper, Ł. Hetmańczyk, R. Podgajny, *Chem. Eur. J.* 2018, **24**, 16302–16314.
- S<sup>2</sup> A. L. Rheingold, CCDC 1573034: Experimental Crystal Structure Determination, 2017.
- S<sup>3</sup> W. Kohn, L. J. Sham, *Phys. Rev.* 1965, **140**, A1133–A1138.
- S<sup>4</sup> E. Runge, E. K. U. Gross, *Phys. Rev. Lett.* 1984, **52**, 997–1000.
- S<sup>5</sup> J. Kobylarczyk, D. Pinkowicz, J. Hooper, M. Srebro-Hooper, R. Podgajny, *Dalton Trans.* 2017, **46**, 3482–3491.
- S<sup>6</sup> J. Kobylarczyk, D. Pinkowicz, J. Hooper, M. Srebro-Hooper, R. Podgajny, *Cryst. Growth Des.* 2019, **19**, 1215–1225.
- S<sup>7</sup> E. Kuzniak, J. Hooper, M. Srebro-Hooper, J. Kobylarczyk, M. Dziurka, B. Musielak, D. Pinkowicz, J. Raya, S. Ferlay, R. Podgajny, *Inorg. Chem. Front.* 2020, **7**, 1851–1863.
- S<sup>8</sup> a) G. Kresse, J. Hafner, *Phys. Rev. B* 1993, **47**, 558–561; b) G. Kresse, J. Furthmeller, *Phys. Rev. B* 1996, **54**, 11169–11186.
- S<sup>9</sup> a) P. E. Blöchl, *Phys. Rev. B* 1994, **50**, 17953–17979; b) G. Kresse, D. Joubert, *Phys. Rev. B* 1999, **59**, 1758–1775.
- S<sup>10</sup> a) J. P. Perdew, K. Burke, M. Ernzerhof, *Phys. Rev. Lett.* 1996, **77**, 3865–3868; b) J. P. Perdew, K. Burke, M. Ernzerhof, *Phys. Rev. Lett.* 1997, **78**, 1396–1396.
- S<sup>11</sup> S. Grimme, J. Antony, S. Ehrlich, J. Krieg, *J. Chem. Phys.* 2010, **132**, 154104.
- S<sup>12</sup> S. Grimme, S. Ehrlich, L. Goerigk, *J. Comput. Chem.* 2011, **32**, 1456–1465.
- S<sup>13</sup> A. I. Liechtenstein, V. I.; Anisimov, J. Zaanen, *Phys. Rev. B* 1995, **52**, R5467–R5470.
- S<sup>14</sup> A. Krukau, O. Vydrov, A. Izmaylov, G. Scuseria, *J. Chem. Phys.* 2006, **125**, 224106.
- S<sup>15</sup> Tang, W.; Sanville, E.; Henkelman, G. *J. Phys. Condens. Matter* 2009, **21**, 084204.
- S<sup>16</sup> a) Mitoraj, M.; Michalak, A. *J. Mol. Model.* 2007, **13**, 347–355; b) Mitoraj, M. P.; Michalak, A.; Ziegler, T. *J. Chem. Theory Comput.* 2009, **5**, 962–975.
- S<sup>17</sup> a) ADF2017, SCM Theoretical Chemistry, Vrije Universiteit, Amsterdam, The Netherlands, <http://www.scm.com>; b) C. Fonseca Guerra, J. G. Snijders, G. te Velde, E. J. Baerends, *Theor. Chem. Acc.* 1998, **99**, 391–403; c) G. te Velde, F. M. Bickelhaupt, E. J. Baerends, C. Fonseca Guerra, S. J. A. van Gisbergen, J. G. Snijders, T. Ziegler, *T. J. Comput. Chem.* 2001, **22**, 931–967.
- S<sup>18</sup> a) A. D. Becke, *J. Chem. Phys.* 1993, **98**, 5648–5652; b) C. Lee, W. Yang, R. G. Parr, *Phys. Rev. B* 1988, **37**, 785–789; c) S. H. Vosko, L. Wilk, M. Nusair, *Can. J. Phys.* 1980, **58**, 1200–1211; d) P. J. Stephens, F. J. Devlin, C. F. Chabalowski, M. J. Frisch, *J. Phys. Chem.* 1995, **98**, 11623–11627.
- S<sup>19</sup> a) E. van Lenthe, E. J. Baerends, J. G. Snijders, *J. Chem. Phys.* 1993, **99**, 4597–4610; b) E. van Lenthe, E. J. Baerends, J. G. Snijders, *J. Chem. Phys.* 1994, **101**, 9783–9792.
- S<sup>20</sup> a) TURBOMOLE V7.3 2018, a development of University of Karlsruhe and Forschungszentrum Karlsruhe GmbH, 1989–2007, TURBOMOLE GmbH, since 2007; available from <http://www.turbomole.com>; b) R. Ahlrichs, M. Bär, M. Häser, H. Horn, C. Kölmel, *Chem. Phys. Lett.* 1989, **162**, 165–169; c) F. Furche, R. Ahlrichs, C. Hättig, W. Klopper, M. Sierka, F. Weigend, F. *WIREs Comput. Mol. Sci.* 2014, **4**, 91–100.
- S<sup>21</sup> a) A. D. Becke, *Phys. Rev. A* 1988, **38**, 3098–3100; b) J. P. Perdew, *Phys. Rev. B* 1986, **33**, 8822–8824; c) J. P. Perdew, *Phys. Rev. B* 1986, **34**, 7406.
- S<sup>22</sup> F. Weigend, R. Ahlrichs, *Phys. Chem. Chem. Phys.* 2005, **7**, 3297–3305.
- S<sup>23</sup> D. Andrae, U. Häußermann, M. Dolg, H. Stoll, H. Preuß, *Theoret. Chim. Acta* 1990, **77**, 123–141.
- S<sup>24</sup> J. Tomasi, B. Mennucci, R. Cammi *Chem. Rev.* 2005, **105**, 2999–3094.
- S<sup>25</sup> A. Klamt, G. Schüürmann *J. Chem. Soc. Perkin Trans.* 1993, **2**, 799–805.
- S<sup>26</sup> Gaussian 16, Revision C.01, M. J. Frisch, G. W. Trucks, H. B. Schlegel, G. E. Scuseria, M.

---

A. Robb, J. R. Cheeseman, G. Scalmani, V. Barone, G. A. Petersson, H. Nakatsuji, X. Li, M. Caricato, A. V. Marenich, J. Bloino, B. G. Janesko, R. Gomperts, B. Mennucci, H. P. Hratchian, J. V. Ortiz, A. F. Izmaylov, J. L. Sonnenberg, D. Williams-Young, F. Ding, F. Lipparini, F. Egidi, J. Goings, B. Peng, A. Petrone, T. Henderson, D. Ranasinghe, V. G. Zakrzewski, J. Gao, N. Rega, G. Zheng, W. Liang, M. Hada, M. Ehara, K. Toyota, R. Fukuda, J. Hasegawa, M. Ishida, T. Nakajima, Y. Honda, O. Kitao, H. Nakai, T. Vreven, K. Throssell, J. A. Montgomery Jr., J. E. Peralta, F. Ogliaro, M. J. Bearpark, J. J. Heyd, E. N. Brothers, K. N. Kudin, V. N. Staroverov, T. A. Keith, R. Kobayashi, J. Normand, K. Raghavachari, A. P. Rendell, J. C. Burant, S. S. Iyengar, J. Tomasi, M. Cossi, J. M. Millam, M. Klene, C. Adamo, R. Cammi, J. W. Ochterski, R. L. Martin, K. Morokuma, O. Farkas, J. B. Foresman, D. J. Fox, Gaussian, Inc., Wallingford CT, 2016.

S<sup>27</sup> T. Yanai, D. P. Tew, N. C. Handy, *Chem. Phys. Lett.* 2004, **393**, 51–57.

S<sup>28</sup> M. Cossi, V. Barone, *J. Chem. Phys.* 2001, **115**, 4708–4717.

S<sup>29</sup> GaussView, Version 5, R. Dennington, T. A. Keith, J. M. Millam, Semichem Inc., Shawnee Mission, KS, 2009.